



**HAL**  
open science

# MAVEN Observations of Solar Wind-Driven Magnetosonic Waves Heating the Martian Dayside Ionosphere

C. M. Fowler, L. Andersson, R. E. Ergun, Y. Harada, T. Hara, G. Collinson,  
W. K. Peterson, J. Espley, J. Halekas, J. Mcfadden, et al.

► **To cite this version:**

C. M. Fowler, L. Andersson, R. E. Ergun, Y. Harada, T. Hara, et al.. MAVEN Observations of Solar Wind-Driven Magnetosonic Waves Heating the Martian Dayside Ionosphere. *Journal of Geophysical Research Space Physics*, 2018, 123, pp.4129-4149. 10.1029/2018JA025208 . insu-03678216

**HAL Id: insu-03678216**

**<https://insu.hal.science/insu-03678216>**

Submitted on 25 May 2022

**HAL** is a multi-disciplinary open access archive for the deposit and dissemination of scientific research documents, whether they are published or not. The documents may come from teaching and research institutions in France or abroad, or from public or private research centers.

L'archive ouverte pluridisciplinaire **HAL**, est destinée au dépôt et à la diffusion de documents scientifiques de niveau recherche, publiés ou non, émanant des établissements d'enseignement et de recherche français ou étrangers, des laboratoires publics ou privés.

Copyright

## RESEARCH ARTICLE

10.1029/2018JA025208

## MAVEN Observations of Solar Wind-Driven Magnetosonic Waves Heating the Martian Dayside Ionosphere

## Key Points:

- Magnetosonic waves are observed to propagate from the magnetosheath into the dayside Martian ionosphere
- Magnetosonic waves are observed to drive large variations in ionospheric density and temperature
- Wave energy is absorbed by the dense  $O_2^+$  ionosphere, leading to significant ion heating and substantial ionospheric erosion

## Correspondence to:

C. M. Fowler,  
 christopher.fowler@asp.colorado.edu

## Citation:

Fowler, C. M., Andersson, L., Ergun, R. E., Harada, Y., Hara, T., Collinson, G., et al. (2018). MAVEN observations of solar wind-driven magnetosonic waves heating the Martian dayside ionosphere. *Journal of Geophysical Research: Space Physics*, 123, 4129–4149. <https://doi.org/10.1029/2018JA025208>

Received 8 JAN 2018

Accepted 8 APR 2018

Accepted article online 20 APR 2018

Published online 16 MAY 2018

C. M. Fowler<sup>1</sup> , L. Andersson<sup>1</sup> , R. E. Ergun<sup>1</sup> , Y. Harada<sup>2</sup> , T. Hara<sup>3</sup> , G. Collinson<sup>4</sup> , W. K. Peterson<sup>1</sup> , J. Espley<sup>4</sup> , J. Halekas<sup>2</sup> , J. Mcfadden<sup>3</sup>, D. L. Mitchell<sup>3</sup> , C. Mazelle<sup>5</sup> , M. Benna<sup>4</sup> , and B. M. Jakosky<sup>1</sup> 

<sup>1</sup>Laboratory of Atmospheric and Space Sciences, University of Colorado Boulder, Boulder, CO, USA, <sup>2</sup>Department of Physics And Astronomy, University Of Iowa, Iowa City, IA, USA, <sup>3</sup>Space Sciences Laboratory, University of California, Berkeley, CA, USA, <sup>4</sup>NASA Goddard Space Flight Center, Greenbelt, MD, USA, <sup>5</sup>IRAP, University of Toulouse, CNRS, UPS, CNES, Toulouse, France

**Abstract** We present Mars Atmosphere and Volatile Evolution (MAVEN) observations of large-amplitude magnetosonic waves propagating through the magnetosheath into the Martian ionosphere near the subsolar point on the dayside of the planet. The observed waves grow in amplitude as predicted for a wave propagating into a denser, charged medium, with wave amplitudes reaching 25 nT, equivalent to ~40% of the background field strength. These waves drive significant density and temperature variations (~20% to 100% in amplitude) in the suprathermal electrons and light ion species ( $H^+$ ) that correlate with compressional fronts of the magnetosonic waves. Density and temperature variations are also observed for the ionospheric electrons, and heavy ion species ( $O^+$  and  $O_2^+$ ); however, these variations are not in phase with the magnetic field variations. Whistler waves are observed at compressional wave fronts and are thought to be produced by unstable, anisotropic suprathermal electrons. The magnetosonic waves drive significant ion and electron heating down to just above the exobase region. Ion heating rates are estimated to be between 0.03 and 0.2 eVs<sup>-1</sup> per ion, and heavier ions could thus gain escape energy if located in this heating region for ~10–70 s. The measured ionospheric density profile indicates severe ionospheric erosion above the exobase region, and this is likely caused by substantial ion outflow that is driven by the observed heating. The effectiveness of these magnetosonic waves to energize the plasma close to the exobase could have important implications for the long-term climate evolution for unmagnetized bodies that are exposed to the solar wind.

## 1. Introduction

Solar radiation provides a vital energy source for planetary bodies within the solar system. This solar energy heats any gravitationally bound neutral atmosphere and can provide enough energy to ionize individual atoms and molecules, producing a planetary ionosphere. Solar radiation is not the only source of energy output by the Sun; the solar wind is a continuous flow of charged particles emitted radially outward from the solar corona. Although the total power emitted from the Sun in the form of the solar wind is about 6 orders of magnitude less than that of solar radiation, the solar wind can still have significant impact upon planetary ionospheres and atmospheres via the many physical processes that facilitate energy transfer from the solar wind into a planetary system (e.g., Schunk & Nagy, 2009).

Magnetized planets such as Earth possess an internally driven dipole magnetic field that acts to deflect the typically supersonic solar wind flow around the planetary obstacle. This deflection occurs because the solar wind plasma is collisionless, and it cannot readily cross the strong dipole magnetic field. When the upstream solar wind flow is supersonic, a bow shock forms upstream of the planet that converts the kinetic energy of the solar wind into thermal energy in a process known as thermalization (e.g., Papadopoulos, 1971). The solar wind flow behind the shock is subsequently subsonic, and most of the incident solar wind plasma is deflected around the planetary obstacle. At Earth, a nonnegligible fraction of the incident solar wind plasma can, however, gain access to the planetary system by flowing along the magnetic field into the polar cusp regions. This solar wind plasma can deposit its energy into the terrestrial atmosphere via collisions with the neutral

atmosphere (Schunk & Nagy, 2009). Wave-particle interactions can also play an important role in transferring solar wind energy to the terrestrial ionosphere in the cusp regions (e.g., André & Yau, 1997).

Unmagnetized bodies, on the other hand, do not possess a significant dipole magnetic field, and the solar wind interaction with the planetary body can be very different compared to that at Earth, for example. Mars is an example of an unmagnetized body that possesses a gravitationally bound neutral atmosphere and ionosphere. Currents driven in the ionosphere by the incident solar wind produce what is known as an induced magnetosphere, which acts to deflect the solar wind flow about the planetary obstacle (e.g., Bertucci et al., 2011). Because there is no significant dipole field to aid in deflecting the solar wind flow about the planet, the point of pressure balance between the incident solar wind flow and the induced magnetosphere is very close to the planet, typically at distances comparable to the solar wind proton gyroradius (e.g., Edberg et al., 2008; Slavin et al., 1991; Vignes et al., 2000). The Mars-solar wind interaction is subsequently comet like, a description broadly characterized by (1) the body (in this case Mars) possessing a weakly gravitationally bound exosphere that extends far outside of the upstream bow shock, (2) the body lacking any significant internally driven dipole magnetic field, (3) the solar wind proton gyrolength scales being comparable to or greater than the typical standoff distance between the solar wind and the body, and (4) the body possessing a conducting layer (such as a gravitationally bound ionosphere) preventing the solar wind magnetic field from passing directly through the body. Kinetic effects are thus important across the various plasma boundaries at Mars, and as a result, the solar wind is not expected to fully thermalize at Mars before encountering the upper ionosphere and atmosphere. It was predicted that waves and particles from the Mars-solar wind interaction would enable direct energy transfer from the solar wind to the upper atmosphere there (e.g., Cloutier et al., 1969; Cloutier & Daniell, 1979; Ergun et al., 2006; Moses et al., 1988).

Subsequent measurements made by various spacecraft within the Martian ionosphere have provided evidence that this is indeed the case. Magnetometer measurements made by the Mars Global Surveyor (MGS) spacecraft showed that the Mars-solar wind interaction is an ionospheric-atmospheric one, similar to that at Venus (e.g., Bertucci et al., 2005; Cloutier et al., 1999). Analysis of MGS magnetometer data by Brain et al. (2002) and Espley et al. (2006) demonstrated that ultralow frequency (ULF) waves are present upstream of, within, and downstream of, the bow shock and magnetosheath regions at Mars. Mirror mode and magnetosonic waves have also been observed upstream and downstream respectively of the magnetic pileup boundary at Mars by MGS (e.g., Bertucci et al., 2004). Plasma observations made by the Mars EXpress (MEX) spacecraft have also shown the presence of ULF waves in ion and electron energy spectra measured within the magnetosheath and ionosphere (Dubinin & Fraenz, 2016; Lundin et al., 2011; Winningham et al., 2006). Solar wind plasma was also observed by MEX down to low altitudes in the dayside ionosphere, implying that the Martian upper atmosphere is directly subject to solar wind forcing and further demonstrating that the transition between the solar wind plasma and ionospheric plasma is highly dynamic and controlled by the solar wind (Dubinin et al., 2008; Lundin et al., 2004). Upstream solar wind conditions have also been observed to influence ion escape at Mars; enhancements in heavy ion escape rates by factors of up to  $\sim 10$  have been observed to correlate with the occurrence of coronal mass ejections and solar wind pressure pulses (Edberg et al., 2010; Futaana et al., 2008). During more quiet solar wind conditions ion escape tends to be more comet like, consisting of low-energy ions flowing over the terminator and downstream into the Martian magnetotail (Lundin et al., 2008).

More recent measurements made by the Mars Atmosphere and Volatile Evolution (MAVEN) mission support these earlier interpretations. MAVEN is the first dedicated aeronomy mission to Mars and as such is the most capable to date of characterizing the plasma environment within the ionosphere there. Enhancements in electron temperature within the upper dayside ionosphere have been observed to correlate with enhancements in electric field wave power (Fowler, Andersson, Peterson, et al., 2017), and significantly, heated ion populations have also been observed in the middle to upper dayside ionosphere (Fowler, Ergun, et al., 2017). Electric field wave power whose source was assumed to be within the magnetosheath has been observed to penetrate 100–200 km into the dayside upper ionosphere (Fowler, Andersson, Halekas, et al., 2017) and is a possible energy source for these ionospheric energization events.

We present here MAVEN observations of what are interpreted as large-amplitude magnetosonic waves propagating through the dayside magnetosheath and into the dayside upper ionosphere. These waves are likely driven by the solar wind interaction with the planet and cause large density and temperature variations within

the upper ionosphere. Significant ion heating and outflow appear to be associated with these waves that may have substantial implications for atmospheric loss to space and evolution of the Martian climate over time.

The rest of this paper is organized as follows: The data and instrumentation used in this study are described in section 2; time series plasma data of a single magnetosonic wave event is presented in section 3. Discussion and interpretation of the data shown in section 3 are presented in section 4. The results of a small statistical study that highlight the importance of such wave events in the context of atmospheric and climate evolution are discussed in section 5. A general discussion is presented in section 6 before concluding in section 7.

## 2. Data and Instrumentation

The data used in this study were acquired by National Aeronautics and Space Administration's MAVEN mission, which entered Mars orbit in October 2014 (Jakosky et al., 2015). MAVEN is in an elliptical orbit that allows the spacecraft to regularly sample the upstream solar wind at apoapsis (about 6,000-km altitude), before entering the ionosphere and sampling down to about 150-km altitude at periapsis. The instrumentation suite carried by MAVEN is designed to observe the plasma and neutral environment at Mars, and data from the following instruments are used in this study: SupraThermal and Thermal Ion Composition (STATIC, McFadden et al., 2015), Langmuir Probe and Waves (LPW, Andersson et al., 2015), Solar Wind Electron Analyzer (SWEA, Mitchell et al., 2016), Magnetometer (MAG, Connerney, Espley, Lawton, et al., 2015), Solar Wind Ion Analyzer (SWIA, Halekas et al., 2015), and Neutral Gas and Ion Mass Spectrometer (NGIMS, Mahaffy et al., 2015). Science quality data from all of these instruments are obtained from the National Aeronautics and Space Administration Planetary Data System.

STATIC is a top-hat electrostatic analyzer that uses time of flight to obtain ion mass information. It measures ions of energies below 1 eV up to 30 keV, using electrostatic deflectors to obtain a field of view of  $360^\circ \times 90^\circ$ . STATIC data are obtained at a cadence of 4 s. Ion mass and energy spectra presented here were obtained from the Planetary Data System; ion velocity distributions with respect to the local magnetic field were produced using publicly available software written by the STATIC instrument team.

LPW consists of two Langmuir Probes that are each mounted at the end of  $\sim 7$ -m booms, which are separated by an angular distance of about  $110^\circ$ . The instrument can operate in either Langmuir Probe (LP) or waves mode. In LP mode, the instrument measures current-voltage (I-V) characteristics from which the local electron density ( $N_e$ ), temperature ( $T_e$ ), and spacecraft potential are derived, using an enhanced fitting method outlined in Ergun et al. (2015). In waves mode, the instrument measures the 1-D electric field power spectrum from 2 Hz to 2 MHz in quasi-logarithmically spaced frequency bins. For the data presented in this study, LPW alternated between LP and waves modes.  $N_e$  and wave spectra are available at a cadence of 4 s.  $T_e$  is available at a cadence of 8 s; the larger cadence for  $T_e$  arises because of differences in surface properties between the two LPW sensors. Sensor 1 has been shown capable of measuring  $T_e$  down to about 525 K, while sensor 2 can measure  $T_e$  as low as about 700 K (Ergun et al., 2015). These lower limits are instrumental, and the electron temperature is expected to be lower than derived values when  $T_e$  approaches these values. Because of this,  $T_e$  from only sensor 1 is used to avoid introducing unreal, wave-like behavior in the  $T_e$  measurements when  $T_e$  from both sensors are used.

SWEA is a hemispherical top-hat electrostatic analyzer that measures electron fluxes from 3 eV to 5 keV. The instrument field of view is provided by electrostatic deflectors, spanning  $360^\circ \times 120^\circ$ . SWEA has an energy resolution of 17% ( $\Delta E/E$ ); pitch angle distributions are produced on ground using publicly available software written by the SWEA instrument team.

MAG measures the 3-D magnetic field vector at 32 Hz. The instrument consists of two fluxgate magnetometers to provide hardware redundancy and to allow for the calibration and removal of spacecraft-generated magnetic fields (Connerney, Espley, DiBraccio, et al., 2015). The instrument has an accuracy better than 0.05% and can measure magnetic fields up to 65,536 nT in strength. Publicly available software written by the MAG instrument team is used to produce magnetic field power spectra on ground, based on the process outlined in Torrence and Compo (1998).

SWIA is an electrostatic top-hat analyzer whose field of view spans  $360^\circ \times 90^\circ$ . SWIA measures ion fluxes from 25 eV to 25 keV in energy, with an energy resolution of 14.5%. Data presented here have a cadence of 4 s.

NGIMS is a mass resolving spectrometer that is able to measure multiple neutral and ion species in quick succession. The measurement cadence for any given species is usually 2–3 s; however, this varies depending on the exact number of species being measured during any single periapsis pass.

### 3. Example Event

#### 3.1. Time Series Plasma Data Observations

MAVEN is able to periodically sample the upstream bow shock, magnetosheath, and dayside upper ionosphere, within the same periapsis pass and all at low solar zenith angles (SZAs), due to the precession of its orbit over time. Low SZA is defined here as below about  $30^\circ$ . These sampling periods occur every few months or so, lasting about 3–4 weeks at a time. An example of an inbound periapsis pass from one such period is shown in Figure 1. The ionospheric electron density and temperature, as measured by LPW, are shown in panels a and b, respectively. The omnidirectional suprathermal electron energy flux measured by SWEA is shown in panel c (efflux has units of  $\text{eV} (\text{eV cm}^2 \text{ s sr})^{-1}$ ). The 3-D magnetic field vector as measured by MAG is shown in panel d in the Mars Solar Orbital (MSO) coordinate system. The MSO frame is defined as X pointing along the Mars-Sun line, sunward; Y points approximately opposite to Mars' orbital motion about the Sun; and Z completes the right-handed orthogonal system. The magnitude of the magnetic field strength is shown as the black line in panel e; the blue line shows the average strength over a 90-s sliding window. The red line shows the modeled magnetic crustal field strength (Morschhauser et al., 2014). The 3-D magnetic field vector in the frame of the magnetic field is shown in panel f; the component  $B_1$  is parallel to the field; components  $B_2$  and  $B_3$  are orthogonal and perpendicular to the field. The method for this rotation is described in section 3.2.

The LPW 1-D electric field power spectrum is shown in panel g and “E power” has units of  $\text{V}^2 \cdot \text{m}^{-2} \cdot \text{Hz}^{-1}$ . Panel g includes both the active and passive wave spectra; the active spectra include wave sounding intended to excite the local plasma line (thus providing another method to derive the local ionospheric electron density), while the passive spectra do not. More details on this can be found in Fowler, Andersson, Halekas, et al. (2017). The horizontal, low-power noise feature at about 500 Hz at all times is a result of signal processing; the large values of electric field wave power across the entire frequency spectrum observed after about 06:01 are noise caused by aliasing within the instrument. These features are also discussed in detail in Fowler, Andersson, Halekas, et al. (2017). The absolute magnetic field wave power spectrum is shown in panel h and “B power” has units of  $\text{T}^2/\text{Hz}$ .

The omnidirectional ion energy spectrum for all ion masses, as measured by STATIC, is shown in panel i. The data in this panel (and all other STATIC ion energy spectra presented in this manuscript) have not been corrected for spacecraft potential effects. The spacecraft potential, as measured by STATIC, is overplotted as the green line in the panel, referenced to the y axis. The corresponding ion mass spectrum from STATIC is shown in panel j. This panel can be used to provide first-order estimates of the ion composition; however, exact ion species densities from this time period are difficult to obtain due to ongoing instrument calibration during this time period. For this study, based on panel j, we assume that protons dominate the ion density before about 05:54:30 UTC;  $\text{O}^+$  dominates between 05:54:30 and about 05:57:30; and  $\text{O}_2^+$  dominates after 05:57:30. Gray regions in panels c, i, and j mark times and energies when counts are below the lower limit of the color bar in each panel. We note that NGIMS is also capable of providing individual ion species densities; however, the instrument did not operate in ion mode during this periapsis and those densities are not available here.

Magnetic field orientation information is shown in panel k. The red line shows the angle between the local zenith direction and magnetic field vector; values of  $0^\circ$  and  $180^\circ$  represent vertically upward and downward pointing magnetic field, respectively;  $90^\circ$  represents horizontal magnetic field. The green line shows the angle between MAVEN's velocity vector and local magnetic field vector. Values of  $0^\circ$  and  $180^\circ$  represent travel along and antiparallel to the magnetic field, respectively. Values of  $90^\circ$  represent travel perpendicularly across the magnetic field. Dotted lines have been added at angles of  $45^\circ$ ,  $90^\circ$ , and  $135^\circ$  in the panel to aid the reader.

The spacecraft position in the MSO frame (in units of Mars radii), the spacecraft altitude in the International Astronomical Union Mars planetocentric frame (in units of kilometers), and the spacecraft SZA (in units of degrees) are shown underneath the bottom panel of the figure.

The spacecraft starts within the magnetosheath at 05:48 UTC with an SZA of about  $26^\circ$ . Shocked, hot electrons are observed by SWEA (panel c), coincident with high-frequency fluctuations in the electric and magnetic fields (panels d, g, and h), which are all characteristics of the magnetosheath. Low ionospheric electron

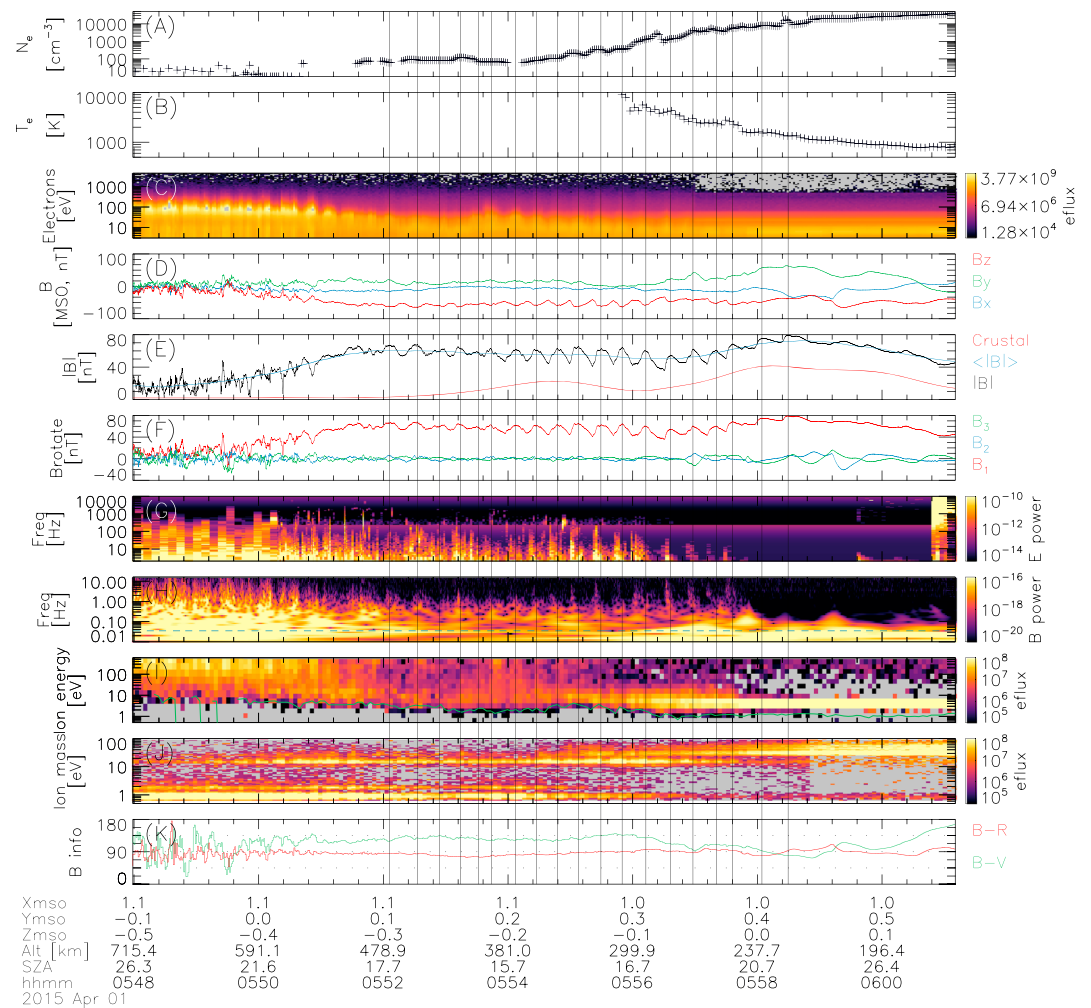


**Figure 1.** Time series plasma data overview of a Mars Atmosphere and Volatile EvolutionN dayside inbound periapsis pass. Panels are the following: (a and b) Langmuir Probe and Wave ionospheric electron density ( $N_e$ ) and temperature ( $T_e$ ); (c) Solar Wind Electron Analyzer omnidirectional suprathermal electron energy flux; (d) Magnetometer 3-D magnetic field vector  $\vec{B}$  in the Mars Solar Orbital (MSO) frame; (e)  $|\vec{B}|$  (black); 90-s average of  $|\vec{B}|$  (blue), crustal magnetic field contribution (red); (f) 3-D magnetic field vector in the magnetic field frame ( $\vec{B}_1$  is parallel to the field;  $\vec{B}_2$  and  $\vec{B}_3$  are orthogonal and perpendicular to the field); (g) Langmuir Probe and Wave 1-D electric field power spectrum; (h) magnetic field power spectrum; (i and j) SupraThermal and Thermal Ion Composition omnidirectional ion energy and mass spectra; (k) angle between the local magnetic field vector and local zenith (red), and angle between the local magnetic field vector and the Mars Atmosphere and Volatile EvolutionN spacecraft velocity vector (green). Black vertical lines mark peaks in  $|\vec{B}|$ . SZA = solar zenith angle.

densities below  $\sim 50 \text{ cm}^{-3}$  are also observed by LPW (panel a); corresponding electron temperatures are not available in panel b because these electron temperatures are too hot to be derived from the measured I-V characteristics. These electrons thus likely overlap with the suprathermal population observed by SWEA in panel c. Panel j shows that protons dominate the ion composition within the sheath, as expected.

At about 05:52 UTC the upper extent of the ionosphere starts to be continuously measured by LPW (panel a), although the electron temperature is still too hot to be derived (panel b). In this region at the upper edge of the ionosphere the ionospheric electron densities measured by LPW and the hot suprathermal electron densities measured by SWEA are comparable (see Figure 2b). The reduction in shocked electron energy flux above  $\sim 100$ -eV energy observed by SWEA (Figure 1c) further indicates the transition from magnetosheath to upper ionosphere. The magnetic field strength during this transition has increased to about 60 nT (Figure 1e), which is atypically large for a draped field configuration (e.g., Bertucci et al., 2003; Brain et al., 2006; Mittelholz et al., 2017). This strong field does not appear to be a result of the presence of strong magnetic crustal fields

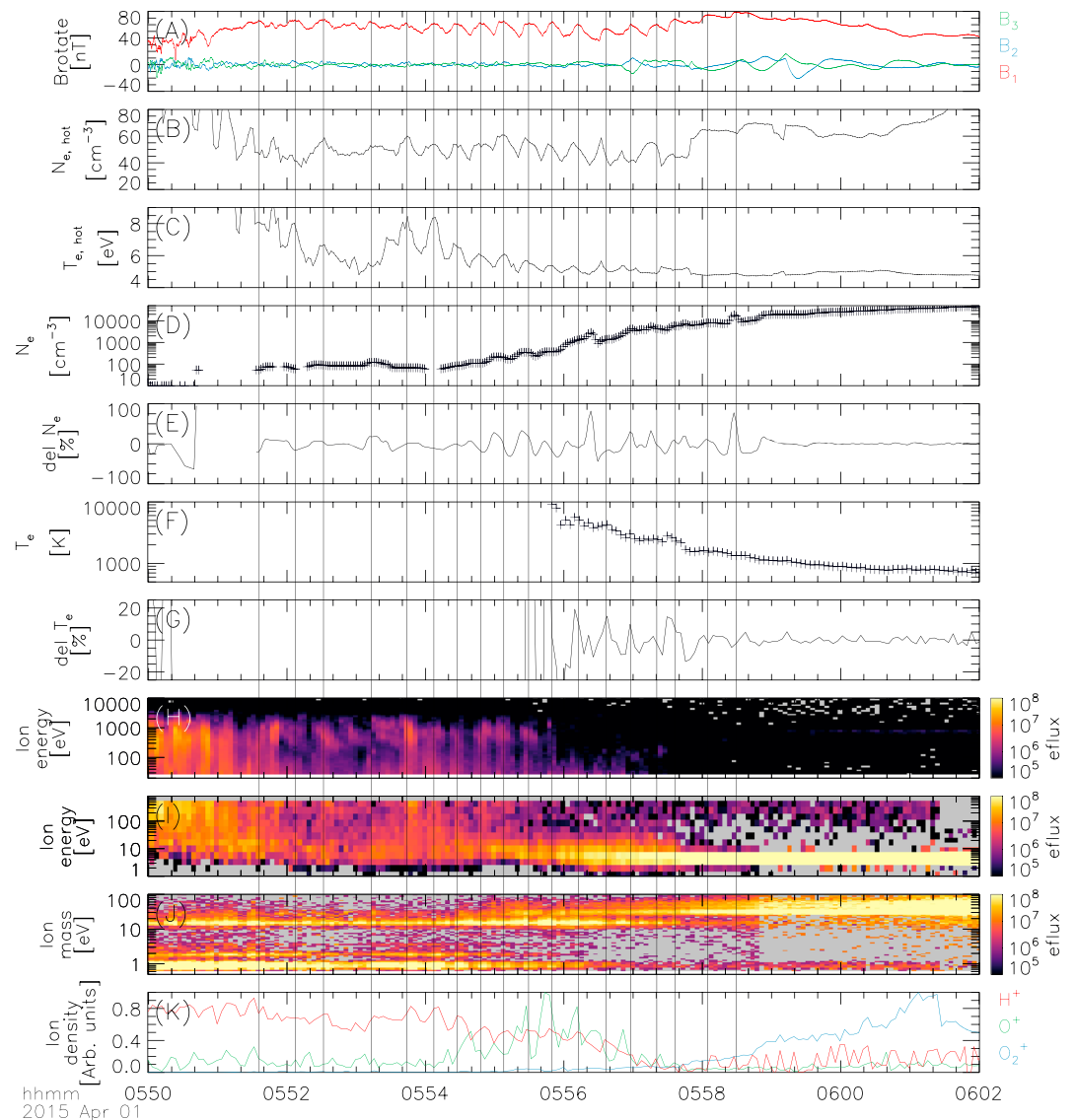


**Figure 2.** Time series plasma data showing large density variations in the upper ionosphere. Panels are the following: (a) 3-D magnetic field vector  $\vec{B}$  in the magnetic field frame; (b and c) suprathermal electron density and temperature; (d and e) Langmuir Probe and Wave  $N_e$ , and variations of  $N_e$ ; (f and g) Langmuir Probe and Wave  $T_e$ , and variations of  $T_e$ ; (h) Solar Wind Ion Analyzer omnidirectional ion energy spectrum; (i and j) SupraThermal and Thermal Ion Composition omnidirectional energy and mass spectra; (k) relative ion densities for  $H^+$ ,  $O^+$ , and  $O_2^+$  in arbitrary units (see main text). Black vertical lines mark peaks in  $|\vec{B}|$ .

(red line, panel e) until about 05:54. At 05:52, longer period oscillations at about 0.03–0.05 Hz start to become clear in the magnetic field data (panels d and e) and also the magnetic field power spectrum (panel h). Panel f shows that these oscillations are purely in the parallel component of the field, suggesting that these are compressional in nature. Upon careful inspection of panel h, this wave signature can be tentatively traced back to the magnetosheath region; the horizontal dashed blue line in panel h marks a frequency of 0.035 Hz, and wave-like signatures at this frequency are observed back into the magnetosheath region. Corresponding variations in the SWEA and STATIC data (panels c, i, and j) at similar frequencies are also observed in the magnetosheath. For the remainder of this paper, the magnetic variations observed between  $\sim 0.03$  and 0.05 Hz are referred to as the 0.035-Hz variations.

Between 05:52 and about 05:56:30 the ionospheric density increases to about  $10^4 \text{ cm}^{-3}$  (panel a) and the ionospheric composition transitions to mainly  $O^+$  (panel i). The ionospheric electron temperature is still too high to be derived from the LPW measurements at the start of this region, suggesting that the ionospheric

plasma is still hot there and this is supported by the energetic ions observed by STATIC at energies up to several hundreds of electron volts (panel i). The  $\sim 0.035$ -Hz oscillations in the magnetic field increase in amplitude to about 20–25 nT and are coincident with variations in other plasma parameters. The vertical black lines in the figure mark obvious peaks in the magnetic field strength, to aid with comparison to other panels. Note that these peaks in magnetic field strength can be identified out into the magnetosheath but with less confidence and as such we only mark the most obvious peaks here. As is discussed in section 3.3, variations in the suprathermal electron population and light ion species densities correlate with peaks in the magnetic field strength, while the ionospheric electron and heavy ion densities do not correlate with variations in the magnetic field strength. Bursts of enhanced magnetic and electric field wave power are observed centered on these peaks in magnetic field strength (panels g and h). These are likely Whistler mode waves driven by the observed unstable suprathermal electron population, and this is discussed in section 3.4.

After 05:56:30, the amplitudes of the  $\sim 0.035$ -Hz waves, and coincident variations in electron and ion densities and temperatures, begin to decrease in size, while the ionospheric density continues to increase.  $O_2^+$  becomes the dominant ion species here. The bursts of enhanced magnetic and electric field wave powers observed centered on the peaks in magnetic field strength also decrease in amplitude after 05:56:30. These observations suggest that damping of the  $\sim 0.035$ -Hz waves occurs and this energy conversion is discussed in sections 3.5 and 4.

By 06:00 the amplitudes of the compressional waves in the magnetic field are greatly reduced, and there are no obvious variations in ionospheric density or temperature that coincide with the remnant variations in magnetic field strength. Bursts in magnetic and electric field wave power above 1–2 Hz are no longer detected. The magnetic field wave power observed below about 0.1 Hz is frequently observed at these low altitudes in the Martian ionosphere and is likely caused by a combination of magnetic structures and heavy ion cyclotron waves (e.g., Espley et al., 2006).

The spacecraft potential as observed by STATIC is roughly constant between about  $-1$  and  $-2$  V in the deep ionosphere, when the ionospheric density gets above a few hundreds of cubic centimeters. At lower densities (higher altitudes), the potential is larger, reaching about  $-10$  V in the magnetosheath. This behavior is normal, and the spacecraft potential is not discussed further.

The red line in panel k shows that the magnetic field is essentially horizontal throughout the entire pass, meaning that the magnetic field is draped about the dayside of the planet as expected. MAVEN flies across the magnetic field for the entire pass, at an angle of about  $90^\circ$ – $135^\circ$  when the large-amplitude waves are observed in the magnetic field.

### 3.2. Method for Rotating Into the Magnetic Field Frame

Figure 1f shows the 3-D magnetic field vector in the frame of the magnetic field, that is, the component  $B_1$  is parallel to the magnetic field, and the components  $B_2$  and  $B_3$  are orthogonal and perpendicular to the magnetic field. The coordinate rotation is performed on the full resolution 32-Hz 3-D magnetic field vector  $\vec{B}$  shown in Figure 1d, with respect to the spacecraft velocity vector;  $\vec{V} \cdot \vec{B}$  is first smoothed over a 60-s sliding window, to obtain the vector  $\vec{B}_0$ . The component parallel to the magnetic field is obtained by calculating the dot product between the unit vector of the smoothed field,  $\vec{B}_0$ , with  $\vec{B}$ .

The first perpendicular direction to  $\vec{B}_0$ ,  $\vec{B}_1$ , is defined as the cross product  $\vec{B}_0 \times \vec{V}$ . The second perpendicular direction to  $\vec{B}_0$ ,  $\vec{B}_2$ , is defined as  $(\vec{B}_0 \times \vec{V}) \times \vec{B}_0$ . The magnitudes of  $\vec{B}_1$  and  $\vec{B}_2$  are obtained by calculating the dot product between the unit vector of  $\vec{B}_1$  or  $\vec{B}_2$  with  $\vec{B}$ .

The spacecraft velocity vector  $\vec{V}$  changes on time scales much slower than the variations in magnetic field being investigated here ( $\sim 0.035$  Hz) and is thus an appropriate reference vector to perform this rotation with.

### 3.3. Density Variations

To evaluate the observed plasma density variations in the upper ionosphere, time series plasma density variation information is shown in Figure 2. The 3-D magnetic field vector in the magnetic field frame is shown in panel a. The suprathermal electron density and temperature are shown in panels b and c, respectively. The ionospheric electron density, and the variation of this, is shown in panels d and e. The ionospheric electron temperature and its variability are shown in panels f and g. The high energy, omnidirectional ion energy spectrum from SWIA is shown in panel h; the lower energy, ion energy, and mass spectra from STATIC are shown in panels i and j. Individual densities for protons,  $O^+$  and  $O_2^+$ , are shown in panel k in red, green, and blue, respectively. These densities are derived from the STATIC data; however, calibration difficulties during this time

period mean that absolute ion densities are hard to obtain and the densities are thus presented in arbitrary units here. We subsequently focus on relative changes in individual ion species densities and do not compare absolute ion densities. The vertical black lines mark obvious peaks in the compressional waves observed in the magnetic field.

Variations of 20–30% are observed in the suprathermal electron density (panel b); peaks in these variations correlate with peaks in the magnetic field strength, especially above altitudes of about 300 km (i.e., prior to 05:56 UTC), when the ionospheric density (measured by LPW) is still low, at values of a few hundreds of cubic centimeters or less. Similar trends are observed in the suprathermal electron temperature (panel c); temperature variations of up to 15% are observed, and peaks in the temperature correlate with peaks in the magnetic field strength, particularly at higher altitudes. The variations in suprathermal electron density and temperature become less pronounced just before 05:58 UTC, which coincides with when the compressional waves in the magnetic field reduce in amplitude and the ionospheric density starts to become large ( $\sim 10^5 \text{ cm}^{-3}$ ).

Variations in ionospheric electron density (panels d and e) are sometimes correlated, and sometimes uncorrelated, with peaks in the compressional waves observed in the magnetic field. Variations of  $\sim 20$ –100% are, however, observed in electron density down to altitudes of about 220 km ( $\sim 05:59$  UTC), corresponding to ionospheric densities of about  $10^5 \text{ cm}^{-3}$ . Variations in electron temperature (panels f and g), on the other hand, appear more correlated with the compressional waves; variations of about 15% are observed down to similar altitudes. There are no significant variations in ionospheric electron density and temperature below about 200 km, coinciding with times when the compressional wave amplitudes have diminished in size.

Fluctuations in ion density correlate well with variations in the magnetic field when the ion gyrofrequency is greater than the wave frequency ( $\sim 0.035$  Hz). When protons make up a significant fraction of the plasma density, peaks in proton density observed by SWIA and STATIC (panels h, i, and k) correlate well with peaks in the magnetic field strength (particularly between about 05:54 and 05:57:30). For the observed magnetic field strengths of  $\sim 60$  nT, the local proton gyrofrequency is about 1 Hz or 20–30 times larger than the frequency of the observed compressional waves.  $\text{O}^+$  dominates the ion composition between about 05:54:30 and 05:57:30, and peaks in  $\text{O}^+$  density (panel k) only partially correlate with the magnetic field. The corresponding  $\text{O}^+$  gyroperiod is about 0.05–0.06 Hz, comparable to and slightly larger than the frequency of the compressional wave.  $\text{O}_2^+$  dominates the ion composition after about 05:57:30, and no obvious correlations are observed between  $\text{O}_2^+$  densities and the compressional wave fronts (panel k).  $\text{O}_2^+$  has a corresponding gyroperiod of about 0.02–0.03 Hz, comparable to but slightly less than the compressional wave frequency. This event clearly demonstrates how the lighter ion species move with the magnetic field, but the heavier species do not.

### 3.4. Whistler Wave Generation

The electric and magnetic field power spectra presented in Figure 1 show bursts of enhanced wave powers centered on the peaks of the compressional waves observed in the magnetic field. These enhancements are clearly present above about 1 Hz in the magnetic field data and above 2 Hz in the LPW electric field spectra (note that the LPW spectra are not available below 2 Hz and these enhancements may exist at lower frequencies in the electric field as well). Time series plasma data shown in Figure 3 present these observations in more detail. The 3-D magnetic field vector in the frame of the magnetic field is shown in Panel a. The SWEA omnidirectional suprathermal electron energy flux is shown in panel b. The ratio of perpendicular ( $T_{\perp}$ ) to parallel ( $T_{\parallel}$ ) suprathermal electron temperature, relative to the local magnetic field vector, is shown in panel c; the horizontal line shows a value of 1 where the temperature components are equal. These temperature components are derived using software provided by the SWEA instrument team, for the energy range 3 eV–5 keV. The magnetic and electric field power spectra are shown in panels d and e, respectively. The two white lines overplotted on the electric field power spectrum show the electron cyclotron (top) and lower hybrid (bottom) frequencies, derived using the suprathermal electron density and local magnetic field strength. The proton cyclotron frequency lies just below 1 Hz. The suprathermal electron pitch angle distribution for electrons spanning 50–100 eV in energy is shown in panel f. The vertical black lines in the figure mark obvious peaks in magnetic field strength.

The ratio of  $T_{\perp}$  to  $T_{\parallel}$  (Figure 3c) demonstrates that  $T_{\perp}$  is greater than  $T_{\parallel}$  at, or just prior to, peaks in the magnetic field strength. When this ratio is greater than 1, the suprathermal electron pitch angle distribution is anisotropic and the population is unstable to the Whistler wave mode (e.g., Kennel & Petschek, 1966). These times correspond to times when the suprathermal electron pitch angle distribution is enhanced

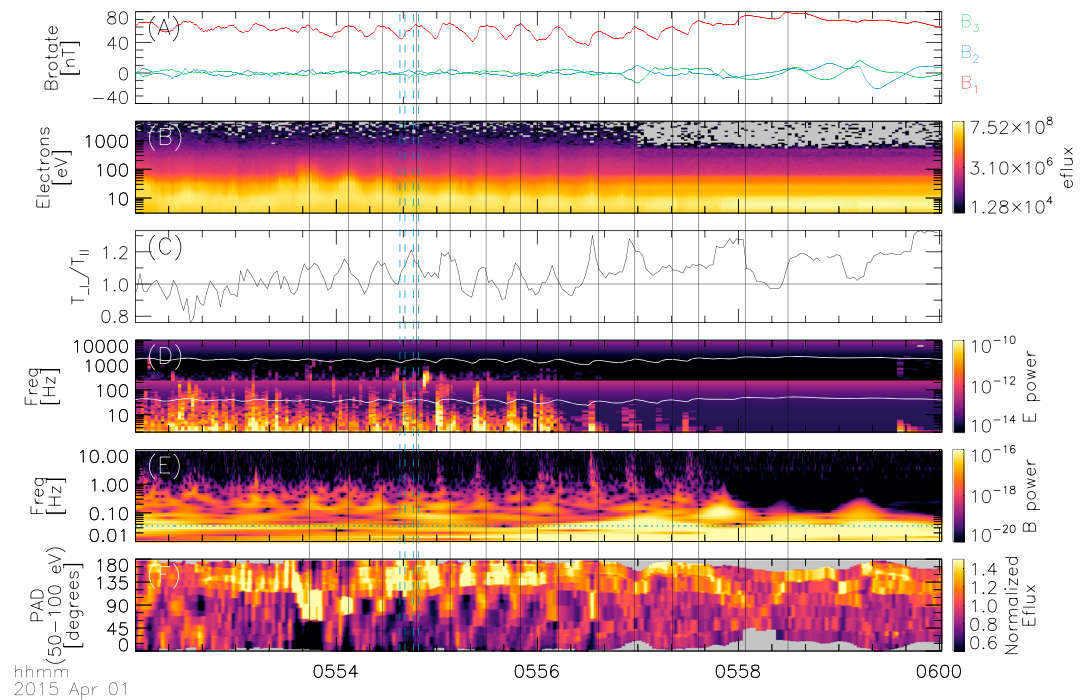


**Figure 3.** Time series plasma data showing the generation of Whistler waves within the ionosphere. Panels are the following: (a) 3-D magnetic field vector  $\vec{B}$  in the magnetic field frame; (b) Solar Wind Electron Analyzer omnidirectional suprathermal electron energy flux; (c) ratio of suprathermal electron  $T_{\perp}$  to  $T_{\parallel}$ ; (d and e) magnetic and electric field power spectra; (f) suprathermal electron pitch angle distributions for the energy range 50–100 eV. Black vertical lines mark peaks in  $|\vec{B}|$ . The two pairs of blue dashed vertical lines mark times from when suprathermal electron energy spectra shown in Figure 4 are taken.

in the perpendicular direction relative to the local magnetic field (i.e., at pitch angles of 60–120° in Figure 3f), suggesting that the compressed magnetic field can drive the suprathermal electrons anisotropic.

Comparison of suprathermal electron energy spectra at times of magnetic field minima and maxima supports the theory that compression of the magnetic field is the likely source of the observed suprathermal electron temperature anisotropy. Example suprathermal electron energy spectra from times of magnetic field minima and maxima are shown in Figures 4a and 4b, respectively. The measurement times of these spectra are marked by the two pairs of blue dashed vertical lines in Figure 3. Figure 4a is measured when the suprathermal electron population is strongly antifield aligned, that is, at pitch angles greater than  $\sim 120^{\circ}$  (Figure 3f). Figure 4b is measured when a significant fraction of suprathermal electron population possesses pitch angles between 60° and 120°. The red (0–60°) and blue (120–180°) distributions are relatively constant between the two panels; however, the green (60–120°) distribution is enhanced during magnetic field compression (panel b), particularly between energies of  $\sim 10$ –100 eV. This population is perpendicular to the local magnetic field and is subsequently interpreted as the likely source driving the enhanced  $T_{\perp}$  during times of magnetic field compression.

### 3.5. Ion Heating

#### 3.5.1. Evidence for Wave Damping and Ion Heating

The effect of the magnetic field fluctuations on ion temperatures can be investigated using ion distributions measured by STATIC. Time series plasma data shown in Figure 5 summarize the derived ion temperatures for the three major ionospheric species  $H^+$ ,  $O^+$ , and  $O_2^+$ . The fitting method used to derive these ion temperatures ( $T_i$ ) is described in Appendix A.

The ionospheric electron density as measured by LPW is shown in panel a of Figure 5; panel b shows the total magnetic field strength in black, with the 90-s average value overplotted in blue and the modeled crustal magnetic field contribution in red. The STATIC ion energy spectrum is shown in panel c.  $H^+$ ,  $O^+$ , and  $O_2^+$  derived ion temperatures are shown in panels d, e, and f, respectively. The green (middle) lines represent the best fit value; the red and blue (upper and lower) lines represent the upper and lower  $T_i$  fit limits.

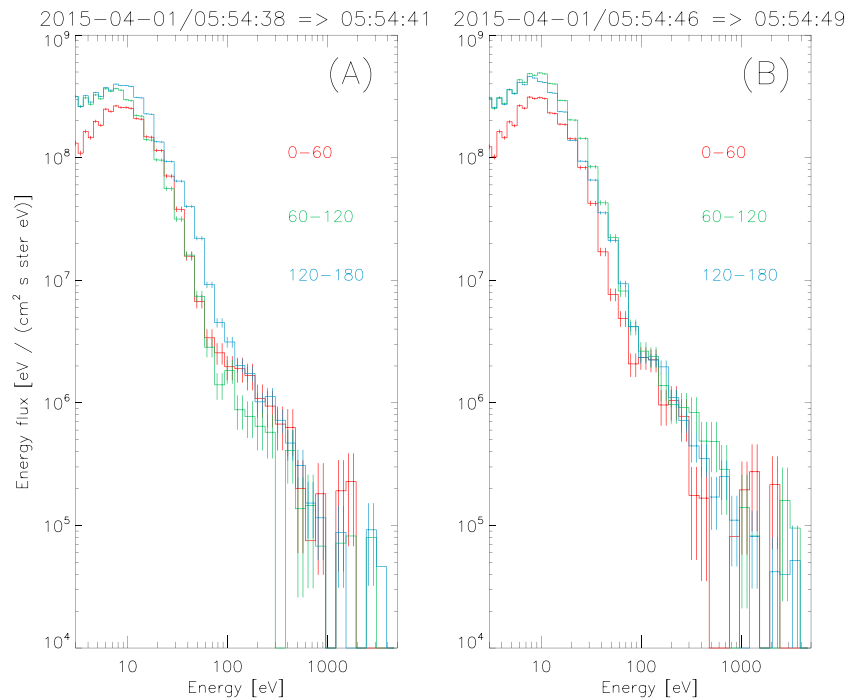


**Figure 4.** Example suprathermal electron energy spectra when the magnetic field is at minimum (panel a) and maximum (panel b) compression. Three different pitch angle ranges are presented: 0–60°, 60–120°, and 120–180° (red, green, and blue, respectively). Electrons traveling antiparallel to the magnetic field (120–180°) dominate in panel a, when Whistler waves are not observed. Electrons gyrating perpendicular to the magnetic field (60–120°) dominate between ~10 and 500 eV in panel b, at times when Whistler waves are observed. Panels a and b are measured during the two sets of vertical dashed blue lines in Figure 3.

The figure covers the time span when MAVEN transitions from the hot shocked plasma of the magnetosheath into the dense ionospheric plasma. Between about 05:50 and 05:52 UTC, shocked plasma is observed by STATIC at high energies, up to several hundreds of electron volts. Panel d shows that the proton-dominated plasma has a  $T_i$  of around 10–20 eV, although hot  $O^+$  and  $O_2^+$  populations also exist with  $T_i$  between 20 and 30 eV (panels e and f). Note that the spike in proton and  $O^+$  temperatures just after 05:52 coincide with when the ionospheric density cannot be derived from LPW measurements (panel a), and a drop in energy flux is observed across all energies by STATIC (panel c). This suggests that the plasma is hot and tenuous and may represent a region of significantly heated ions.

Just prior to 05:52, the 0.035-Hz compressional waves become clearly visible in panel b, and they increase in amplitude until about 05:56. During this time, the ionospheric density increases up to about  $10^4 \text{ cm}^{-3}$  (panel a); STATIC correspondingly observes ions at decreasing energies until the cold ionospheric plasma (at energies below about 10 eV) is observed just prior to 05:58. The derived  $T_i$  for all three ion species on average also decreases between 05:52 and 05:58, as is expected as the plasma density increases.

There is direct evidence that wave power is converted to ion energy, with the best examples observed between 05:56 and just prior to 05:58. Derived  $O^+$  and  $O_2^+$  temperatures increase during this time period, which coincides with when STATIC observes significant energy fluxes at around 10 eV (panel c). The amplitude of the compressional wave observed in the magnetic field also decreases during this time period, and the importance of this is discussed in section 4.

The dash-dot, blue vertical line in Figure 5 marks when the example STATIC ion distribution presented in section 3.5.2 is measured. The four solid, black vertical lines, the dashed green vertical line, and regions 1–3 are discussed in section 4.

### 3.5.2. Example Ion Distribution Functions

Example ion velocity distributions measured by STATIC for  $H^+$ ,  $O^+$ , and  $O_2^+$  are presented in panels a–c of Figure 6. The distributions are measured as the ionospheric electron density starts to rise above  $\sim 100 \text{ cm}^{-3}$ , at about 390-km altitude. Protons still dominate the ion composition here but significant  $O^+$  and  $O_2^+$  densities

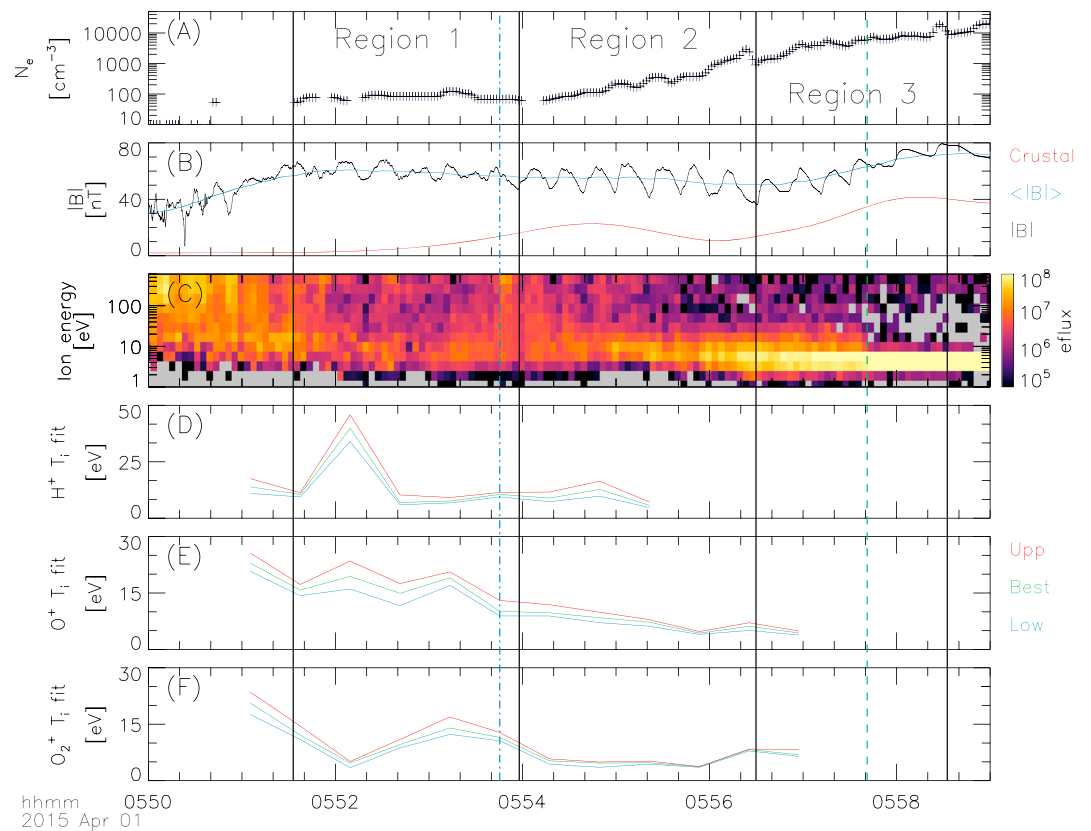


**Figure 5.** Time series plasma data showing heated and energized ion populations in the ionosphere. Panels are the following: (a) Langmuir Probe and Wave  $N_e$ ; (b)  $|\mathbf{B}|$  (black); 90-s average of  $|\mathbf{B}|$  (blue), crustal magnetic field contribution (red); (c) SupraThermal and Thermal Ion Composition omnidirectional ion energy spectrum; (d–f) ion temperatures  $T_i$  derived from SupraThermal and Thermal Ion Composition ion velocity distributions. Green line is the best fit value; red and blue are the upper and lower fit limits. The blue dash-dot vertical line marks when the example ion velocity distributions are shown from in Figure 6. The solid black and green dashed vertical lines define various plasma regions that are discussed in section 4.4.

also exist. The horizontal axes in these panels represent ion velocity parallel to the magnetic field, where positive values are in the field direction. Vertical axes represent ion velocity perpendicular to the magnetic field. The distributions have been corrected for spacecraft motion through the ionosphere, and for spacecraft potential (as observed by STATIC). The plasma is assumed gyrotropic so that all perpendicular velocities are positive. The gray dots in each panel mark individual STATIC measurements within ion velocity space. These points are interpolated onto a regularly spaced 51 by 51 element grid, and this interpolated grid is displayed as the contour plot for each ion species. Ongoing calibration of STATIC data at low energies, below 5 eV, means that these energies are not included in the contour plots. The color bar of each contour plot represents the ion distribution function; the colors for panels a–c are all drawn to the same scale to enable comparison between the different ion species. The time period over which STATIC measures the complete distribution (4 s) is shown at the top of the figure and the dash-dot, blue vertical line in Figure 5 corresponds to the center of this measurement time range. All three ion species show evidence of significant energization perpendicular to the magnetic field.

Panels d–f in Figure 6 show the respective  $T_i$  fits from panels a–c (i.e., panel d pairs with a, e with b, and f with c). The horizontal axes represent ion energy; the vertical axes represent the natural logarithm of the distribution function. The solid black lines represent the distribution function along the edge of the conic marked by the black line in the ion distribution contour plots. The vertical dashed lines encompass the data points used in deriving  $T_i$ , which are the blue crosses marked on the distribution contours.

The green lines in panels d–f show the  $T_i$  best fit values; the red and blue lines show estimates of the upper and lower temperature limits, respectively, in units of electron volt. STATIC measured 12 sets of ion velocity

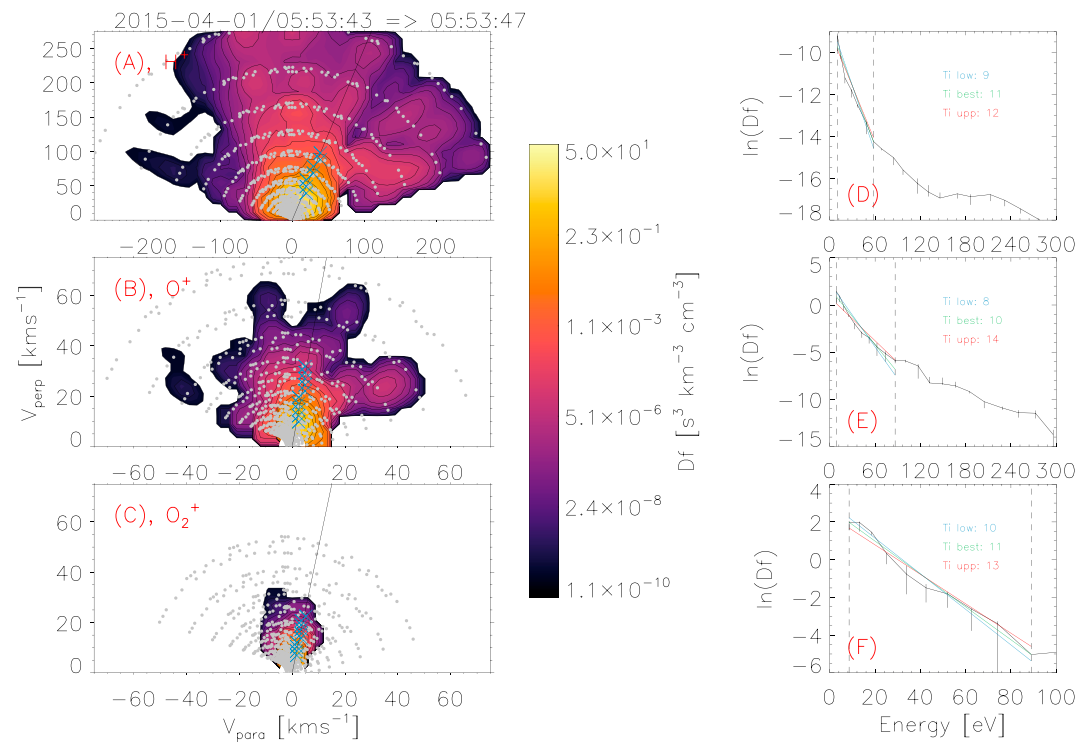


**Figure 6.** Example ion velocity distributions observed by SupraThermal and Thermal Ion Composition assuming gyrotropy, with corrections applied to account for spacecraft velocity and potential. Panels a–c show velocity distributions for individual ion species; the horizontal axes are ion velocity parallel to the magnetic field, and the vertical axes are ion velocity perpendicular to the magnetic field. The gray dots mark SupraThermal and Thermal Ion Composition measurements in velocity space; the contour plot shows an interpolation of these measurements onto a regularly spaced  $51 \times 51$  element grid. Panels d–f show the corresponding ion distribution functions from the interpolated grids, along the ridge of each conic. The best fit ion temperatures (fitted to the blue crosses in the left-hand panels), along with lower and upper limits, are overplotted in these panels in units of electron volt. See section 3.5.2 and Appendix A for more information. The distributions shown here were measured at an altitude of 390 km.

distributions during the time period covered by Figure 5 and a summary of the derived  $T_i$  from all 12 distributions are shown in Figures 5d–5f.

Interestingly, the distribution functions shown in Figures 6a–6c show evidence that energized ions are traveling (with large pitch angles) in both directions along the magnetic field. The solid black line in each panel (a–c) marks the most obvious ridge in the distribution, and these were all in the positive magnetic field direction. Ridges are also apparent in the distributions (particularly for protons and O<sup>+</sup>) at equal pitch angles but in the negative magnetic field direction, suggesting that ions are traveling in both directions along the magnetic field. These features are not the focus of this study and are only briefly discussed in section 4.4.

## 4. Interpretation and Discussion

### 4.1. Magnetosonic Wave Modes

As MAVEN transitions from the magnetosheath into the upper ionosphere (Figure 1, ~05:50–05:52), the magnetic field strength increases to about 60 nT. The modeled crustal field contribution (Figure 1e) is small at first, and this large field strength appears to initially be caused by significant draping of the interplanetary magnetic field about the planetary obstacle. During the transition to the upper ionosphere, low frequency, ~0.035-Hz waves become apparent in the magnetic field data (Figures 1d and 1e), which grow in amplitude as the wave is observed deeper in the ionosphere, up to amplitudes of 20–25 nT. These waves are observed primarily in the parallel component of the magnetic field (Figure 1f), and these are subsequently interpreted as magnetosonic waves. The magnetic field has a strong  $B_z$  component in the MSO frame (Figure 1d), and the magnetic field is aligned in an approximately north-south configuration in the MSO frame. The compressional nature of the magnetosonic wave mode means that the wave will propagate perpendicular to the field direction, which in this case will lead to propagation approximately in the X MSO direction, that is,

**Table 1**  
Summary of Plasma Parameters From the Three Regions Marked in Figure 5

	$N_i$ ( $\text{cm}^{-3}$ )	Ion composition	$T_e$ (K)	$\rho$ ( $\text{kg/m}^3$ )	$ B $ (nT)	$\text{dB}$ (nT)	$V_A$ (km/s)	$V_S$ (km/s)	$E_f$ ( $\text{Jm}^2/\text{s}$ )	Alt (km)
Region 1	80	$\frac{2}{3}\text{H}^+, \frac{1}{3}\text{O}^+$	$2 \times 10^4$	$8 \times 10^{-19}$	60	10	60	6	$1 \times 10^{-6}$	503–383
Region 2a	$10^2$	$\text{O}^+$	$2 \times 10^4$	$3 \times 10^{-18}$	50	14	27	4	$1 \times 10^{-6}$	382
Region 2b /Region 3a	$10^3$	$\text{O}^+$	4,000	$3 \times 10^{-17}$	50	25	9	2	$1 \times 10^{-6}$	282
Region 3b	$10^4$	$\text{O}_2^+$	1,350	$3 \times 10^{-16}$	80	5	4	1	$2 \times 10^{-8}$	224

Note. Parameters are roughly constant in region 1 but vary in regions 2 and 3; subregions a and b subsequently correspond to the start and ends of regions 2 and 3. The columns are, left to right, ionospheric electron density ( $N_e$ ), primary ion composition, ionospheric electron temperature ( $T_e$ ), ionospheric mass density ( $\rho$ ), magnitude of magnetic field strength ( $|B|$ ), size of variations in magnetic field strength associated with the observed magnetosonic wave (dB), Alfvén velocity ( $V_A$ ; which is approximately equal to the wave group velocity here), sound speed ( $V_S$ ), energy flux carried by the wave ( $E_f$ ), altitude range of region 1, or altitude at each region boundary.

planetward or antiplanetward. The upstream solar wind is an obvious energy source to drive these waves planetward, and we believe that this is the case. Waves produced upstream of the shock propagate planetward through the magnetosheath and into the upper ionosphere, and this is supported by the observations shown here. Magnetic field wave power at  $\sim 0.035$  Hz can be traced from the upper ionosphere back into the magnetosheath region (Figure 1h); SWIA and STATIC energy fluxes also show corresponding variations at similar frequencies within the magnetosheath (Figures 2h and 2i).

A more detailed analysis of similar magnetosonic waves observed by MAVEN propagating from the Martian foreshock region through the magnetosheath and into the ionosphere is under preparation.

A simple estimation of the wavelengths of the magnetosonic waves observed in this study can be made using the noted Alfvén speeds in Table 1 (which is introduced in detail in section 4.4) and a frequency of 0.035 Hz. Estimated wavelengths range from  $\sim 1,700$  km in the upper ionosphere down to  $\sim 100$  km in the dense ionosphere. Such wavelengths are significantly larger than the typical gradient length scales of the Martian ionosphere, and it is probably not correct to think of these waves as a wave train propagating through the ionosphere. We instead envision these waves as a series of individual wave fronts “crashing” through the ionosphere, much like a wave breaking on a beach.

Wave and particle interactions between the solar wind interaction region at Mars (i.e., the bow shock and magnetosheath) and the upper dayside ionosphere have been predicted by earlier work (e.g., Ergun et al., 2006; Moses et al., 1988), and we believe that the presented observations show a strong coupling between the upstream solar wind and upper Martian ionosphere. Various observations of what are likely ULF wave-driven phenomena have been previously reported at Mars, based on the analysis of MGS and MEX data, and the presented MAVEN observations strongly support these earlier interpretations. Examples of earlier work include reports of oscillations in ion and electron energy spectra at ULF frequencies within the Martian magnetosheath and ionosphere (Lundin et al., 2011; Winningham et al., 2006), magnetosonic waves just downstream of the magnetic pileup boundary (Bertucci et al., 2004; 2005), and “sawtooth” wave features observed in the magnetic field (Halekas et al., 2011) within the ionosphere. The limited plasma packages carried by MGS and MEX have meant that a complete quantification of the interaction of these wave phenomenon with the Martian ionosphere has not been possible up until now.

#### 4.2. Variations in Ionospheric Density and Temperature

Typical plasma conditions in the upper ionosphere mean that the magnetosonic wave group velocity is much greater than the spacecraft velocity there, and one can assume that the magnetosonic wave frequency is approximately equal to the wave frequency as measured in the spacecraft frame, that is,  $\sim 0.035$  Hz. The proton and electron gyrofrequencies are significantly greater than this and are thus expected to adiabatically respond to variations in magnetic field strength, as is shown in Figures 2b and 2k, before about 05:56 UTC.

Heavier ions with gyroperiods less than the magnetosonic wave frequency will be unable to adiabatically respond to the higher-frequency magnetic field fluctuations, and this is best observed when the plasma density is dominated by  $\text{O}^+$  and  $\text{O}_2^+$ , after about 05:56 UTC. At this point in time, the magnetosonic wave decreases in amplitude and variations in heavy ion species densities are not in phase with variations in magnetic field

strength. For the plasma to maintain quasi-neutrality the ionospheric electrons follow the heavy ion fluctuations, meaning that the ionospheric electron density variations are also out of phase with the magnetic field fluctuations.

The variations in plasma density observed here are unlikely to be driven to first order by the neutral atmosphere because collisions between ions and the neutral atmosphere occur infrequently above the Martian exobase. The Martian ionospheric dynamo region (where ions become demagnetized due to frequent collisions with the neutral atmosphere) is typically located below altitudes of about 170–180 km on the dayside (e.g., Riousset et al., 2014), and subsequently, the plasma density variations observed here are likely driven primarily by the wave-particle interactions described above.

### 4.3. Generation of Whistler Wave Modes

Whistler waves are known to be produced in the Martian magnetosphere via cyclotron resonance with anisotropic electrons (Harada et al., 2016), and we believe that similar instabilities may be driven in the event shown here by the propagating magnetosonic wave fronts. The bursts of magnetic and electric field wave powers observed in Figures 3d and 3e, between about 05:54 and 05:58 UTC, are interpreted as Whistler waves. The spectral shape of these bursts matches those characteristic of Whistler waves (i.e., descending tones as a function of time), and the wave bursts lie well below the electron cyclotron frequency, and just below the lower hybrid frequency (Figure 3d), which are also characteristic of Whistler wave modes.

The electron gyrofrequency is much greater than the  $\sim 0.035$ -Hz magnetosonic wave frequency, and as a result electron motion is expected to correlate with changes in the magnetic field strength and orientation. To preserve the magnetic moment the electron pitch angle distribution becomes more perpendicular during magnetic field compression. The observed variations in suprathermal electron pitch angles are possible assuming an invariant magnetic moment under the observed magnetic field conditions.

A cartoon visualization of this interpretation is shown in Figure 7. Each of the panels a–c represents the same portion of the ionosphere but at progressively later points in time. The curved black lines denote the draped magnetic field on the dayside of the planet; the red and blue lines denote the suprathermal electron population observed by SWEA. As the magnetosonic wave propagates through the ionosphere, the draped field lines will compress and uncompress at the frequency of the wave. Weaker magnetic field strength is denoted in panel a, corresponding to a trough in the wave. The suprathermal electron energy spectrum during this time would be similar to that shown in Figure 4a, when SWEA observes primarily field-aligned magnetosheath electrons. As the wave propagates through the ionosphere, the magnetic field strength increases, corresponding to a compressional front of the magnetosonic wave. This is denoted in Figure 7b; the magnetic field has increased in strength, and the suprathermal electron pitch angle distribution has subsequently become less field aligned. The suprathermal electron energy spectrum would be similar to that shown in Figure 4b. Lower magnetic field strengths follow as the wave propagates through the ionosphere, and this is denoted in Figure 7c. Correspondingly, the electron pitch angle distribution has become more field aligned again. This process repeats periodically as each wave front propagates through the ionosphere.

The suprathermal electron pitch angle distribution is anisotropic during times of magnetic field compression, as observed by comparing the perpendicular and parallel temperatures in Figure 3c. The suprathermal electron pitch angle distribution becomes significantly less field aligned during these times of compression, particularly for energies between 50 and 100 eV (Figure 3f). All of these observations are characteristic of Whistler noise generation during times of magnetic field compression (Kennel & Petschek, 1966). Substitution of observed plasma parameters from Figure 3 into equation (2.21) in Kennel and Petschek (1966; see equation (1) below) demonstrates that the suprathermal electron population observed by MAVEN is indeed unstable to producing Whistler noise during the compressional wave fronts:

$$A^- > \frac{1}{\left(\frac{\Omega^-}{\omega}\right) - 1} \quad (1)$$

where  $A^- = (T_{\perp} - T_{\parallel})/T_{\perp} \approx 0.2$ ;  $\Omega^-$  is the electron cyclotron frequency,  $\approx 1,600$  Hz; and  $\omega$  is the Whistler noise frequency,  $\approx 10$  Hz.

It is thus likely that these compressional fronts ultimately produce the observed bursts of Whistler waves; however, the exact generation mechanism is still unclear. Although the observed suprathermal electrons are unstable to producing Whistler noise, estimates of the resonant energy show that electrons with energies

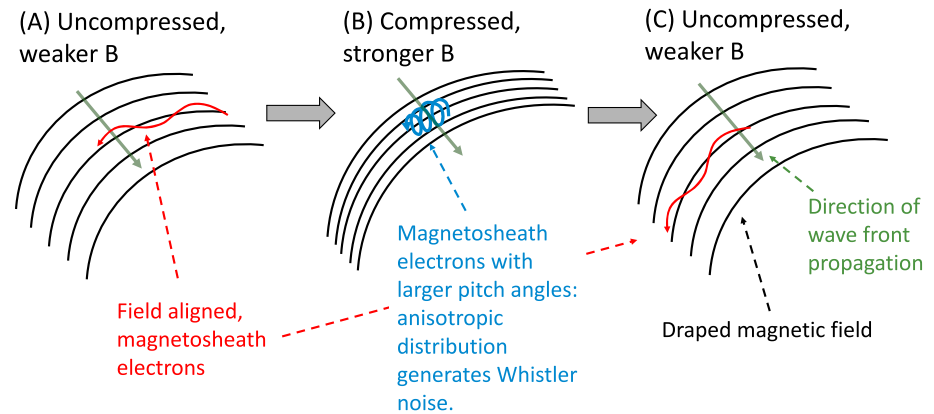


**Figure 7.** Cartoon interpretation demonstrating how the propagation of magnetosonic waves through the ionosphere can lead to unstable suprathermal electron populations that produce the observed Whistler waves. Each panel represents the same portion of the ionosphere, with time increasing a through c. The black curved lines represent the draped magnetic field; the red and blue lines represent suprathermal electrons from the magnetosheath. As the magnetosonic wave propagates through the ionosphere, perpendicular to the magnetic field, the field strength will periodically increase and decrease, as shown in the three panels. Compressions in the field lead to increased electron pitch angles (i.e., the population becomes less field aligned), due to the conservation of the magnetic moment. At these times (denoted in panel b), the ratio of  $T_{\perp}$  to  $T_{\parallel}$  is greater than 1, and the population becomes unstable to the Whistler wave mode.

greater than  $\sim 1$  keV are expected to be the dominant generation source for the observed Whistler bursts. Analysis of the suprathermal electron spectra (e.g., Figure 4b) shows that the density of this high-energy population (energies greater than 1 keV) makes up less than  $\sim 0.01\%$  of the total suprathermal density. The corresponding growth rates (equation (2.20) in Kennel & Petschek, 1966) are subsequently small, and it is unclear whether another mechanism produces the observed Whistler bursts.

#### 4.4. Estimates of Ion Heating Rates in the Ionosphere

Evidence of enhanced ion temperatures is observed in the STATIC energy spectrum down to about 245-km altitude in the ionosphere (Figure 5c), and this time is marked by eye with the vertical dashed green line in Figure 5. Prior to the vertical dashed green line, derived  $T_i$  for all three major ion species ranges between  $\sim 5$  and 30 eV (barring the spike in proton temperature just after 05:52). These enhanced temperatures are likely driven by the magnetosonic wave observed propagating through the ionosphere, and estimates of ion heating rates can be made based on the MAVEN data. The dispersion relation for a magnetosonic wave is given by equation (2) (Schunk & Nagy, 2009):

$$\omega^2 = K^2 \frac{V_S^2 + V_A^2}{1 + \frac{V_A^2}{c^2}} \quad (2)$$

where  $K$  is the wave number;  $V_S$  is the sound speed,  $V_A$  is the Alfvén speed, and  $c$  is the speed of light in a vacuum.  $V_S$  is defined as  $\sqrt{\frac{\gamma k_b T_e}{m_i}}$ ;  $V_A$  as  $\sqrt{\frac{B}{\mu_0 \rho}}$ ; where  $\gamma$  is  $\frac{7}{5}$  for a diatomic gas,  $k_b$  is the Boltzmann constant;  $T_e$  is the electron temperature,  $m_i$  is the ion mass;  $B$  is the magnitude of magnetic field strength,  $\mu_0$  is the permeability of free space; and  $\rho$  is the mass density, defined as  $\sum_i n_i m_i$ , where  $n_i$  is the ion density, and the subscript  $i$  refers to each ion species.

As the magnetosonic wave propagates toward the planet, the wave amplitude is expected to grow if no energy sinks exist. For the observed conditions in the upper Martian ionosphere,  $V_A$  is always at least  $\sim 4$  times larger than  $V_S$ , and  $c \gg V_A$ , and we therefore approximate equation (2) by

$$\omega \approx K V_A \quad (3)$$

The group velocity (defined as  $\frac{\partial \omega}{\partial K}$ ) of the magnetosonic wave is thus approximately equal to  $V_A$ . The energy density carried by the wave is proportional to  $\langle dB \rangle^2$ , where  $\langle dB \rangle$  represents the average amplitude

of the magnetosonic wave. If one assumes that the energy flux carried by the wave is constant (i.e., there are no other sources and sinks of wave energy) then the energy flux  $E_f$  carried by the wave is defined by equation (4):

$$E_f = V_A \frac{\langle dB \rangle^2}{4\mu_0} \quad (4)$$

As the magnetosonic wave propagates into the denser ionosphere, the ionospheric density increases and  $V_A$  subsequently decreases. Thus, as the wave propagates into the ionosphere and  $V_A$  decreases,  $\langle dB \rangle^2$  is expected to increase, if the energy flux carried by the wave is assumed constant. The propagation of the magnetosonic wave into the ionosphere can be evaluated quantitatively using MAVEN data, and this is done with reference to Figure 5. The four solid vertical black lines in Figure 5 mark three different regions within the ionosphere (which are labeled regions 1 through 3 in the figure). Region 1 marks the upper ionosphere when the ionospheric electron density is low and  $V_A$  is large. The ionospheric plasma density remains roughly constant here. Region 2 is characterized by increasing ionospheric densities which are accompanied by increases in the magnetosonic wave amplitudes. Region 3 represents the cold, dense ionosphere, where the magnetosonic wave amplitudes decrease in size and  $O_2^+$  becomes the dominant ion species. Various plasma parameters for these regions are presented in Table 1. These parameters are roughly constant within region 1 but change within regions 2 and 3. Regions 2 and 3 are subsequently characterized by conditions at the start and end of each region, labeled with a and b respectively in the table. The electron temperature was assumed to be  $2 \times 10^4$  K when it was too hot to be derived from LPW measurements in regions 1 and 2a.

If the only energy loss mechanism that the magnetosonic wave is subject to is ion heating, then the wave amplitude in the three regions can be used to estimate the ion heating rates within each region. The estimated energy flux carried by the wave through regions 1 and 2 is constant (Table 1), suggesting that very little ion heating occurs in these regions. The wave energy drops by nearly 2 orders of magnitude in region 3, suggesting that significant ion heating occurs here. STATIC data agree with this interpretation, and significantly, heated  $O^+$  and  $O_2^+$  ions are observed during this time period up to the green dashed vertical line in Figure 5. The dominant ion ( $O_2^+$ ) gyroperiod is comparable to and less than the magnetosonic wave frequency, and these ions are thus able to efficiently damp the wave. Ion energy perpendicular to the magnetic field is subsequently expected to increase and this is also observed in STATIC velocity distributions (Figure 6) and derived  $T_i$  (Figures 5d–5f).

The observed behavior suggests that the magnetosonic wave damping is sensitive to the ionospheric composition, and the greatest damping occurs when the gyroperiods of the primary ionospheric constituents are less than the frequency of the wave. The ionospheric density likely also plays a role in determining the damping rate of the wave; quantitative evaluation of the effects of ionospheric density versus composition, on the damping rate of the wave, is left to future work.

The STATIC energy spectrum shows that the magnetosonic wave likely heats ions at all altitudes (Figure 5c); however, protons and  $O^+$  dominate the composition at higher altitudes and in smaller densities and will not absorb a significant portion of the wave energy there. Large ion energies and temperatures are observed at higher altitudes because ions energized at lower altitudes will continue to be heated by the wave if they flow out of the ionosphere. Energetic protons are typically observed at the transition between the upper ionosphere and magnetosheath, and it is unclear exactly how much of their energy is provided by the magnetosonic wave, given that their gyroperiod is significantly greater than 0.035 Hz throughout this transition.

Because the wave damping occurs in region 3, we assume that the wave loses its energy between region 3a and the dashed vertical green line in Figure 5, past which STATIC no longer observes significantly heated ions. The dashed green line marks an altitude of  $\sim 245$  km and an ionospheric density of  $6 \times 10^3 \text{ cm}^{-3}$ . The heating region is thus assumed to span an altitude depth of roughly 35 km. We assume that this region absorbs all of the wave energy flux entering region 3a ( $3 \times 10^{-7} \text{ J} \cdot \text{cm}^{-2} \cdot \text{s}^{-1}$ ). Because the ionospheric density increases throughout region 3, a lower and upper ion heating rate is calculated by assuming that the ionospheric density is constant at either  $10^3$  or  $6 \times 10^3 \text{ cm}^{-3}$ . The estimated lower and upper heating rates per ion are subsequently  $0.03$  and  $0.2 \text{ eVs}^{-1}$ , respectively.

Just prior to the vertical green dashed line in Figure 5, STATIC observes ions up to energies of about 10 eV, and Figures 5e and 5f show that  $O^+$  and  $O_2^+$  ion temperatures lie between about 5 and 10 eV. Given the estimated

heating rates, ions would need to remain in the heating region for about 1 to 6 min to obtain the upper energy limit of 10 eV. Because the escape energy for  $O^+$  at the surface of Mars is about 2 eV, ions could, however, gain escape energy within 10- to 70-s exposure to this heating region.

## 5. Ionospheric Erosion and Escape to Space

To evaluate the importance of the observed ion heating on the ionosphere, the orbit analyzed here was compared with measurements from neighboring orbits. Ionospheric density profiles measured by LPW show that the ionosphere was severely depleted during the analyzed event, suggesting that the observed magnetosonic waves and subsequent ion heating may drive substantial ion outflow. Ionospheric density profiles from 29 neighboring inbound orbit segments (equivalent to about 3 days either side of the event analyzed here) are shown in Figure 8. Panel a shows the ionospheric electron density as measured by LPW as a function of altitude. The gray lines represent orbits where no obvious magnetosonic wave activity was present in the accompanying magnetic field data (determined by eye). The blue lines mark orbits where smaller-amplitude magnetosonic-like waves were present; these had amplitudes in the region of  $< 10$  nT. The red lines mark orbits where large-amplitude magnetosonic-like waves were observed in the magnetic field data; these had amplitudes in the range of 10–25 nT, similar to the event presented here. The green line marks the event shown here, which had magnetosonic wave amplitudes in the range of 20–25 nT. Only the absolute value of the wave amplitudes were considered here; no comparison was made to the background magnetic field strength. Panel b shows the ionospheric electron temperature, as measured by LPW, as a function of altitude. The color code is the same as for panel a. The dashed horizontal lines in panels a and b mark an altitude of 350 km, which is the altitude up to which panel c extends. The total neutral density, as measured by the NGIMS instrument, is shown in panel c and was obtained by summing all of the individual neutral species measured by NGIMS. Species with atomic mass numbers of 4, 14, 16, 28, 40, and 44 were measured by NGIMS. For reference, neutral O and  $CO_2$  are typically the dominant neutral species in the Martian atmosphere. The color coding is again the same as panels a and b. NGIMS neutral data were not available for some orbits and so fewer segments are presented in this panel. Neutral densities below about  $10^5$   $cm^{-3}$  are at the noise level of the NGIMS instrument and can be interpreted as no significant neutral atmosphere. The inbound orbit segment coverage, as projected on the Y-Z MSO plane, is shown in panel d. The concentric dashed rings mark SZA of  $10^\circ$ ,  $30^\circ$ , and  $60^\circ$ ; the color bar denotes altitude. The coverage of each orbit segment evolves with time due to the precession of MAVEN's orbit. The event shown in this study is marked by the solid black line in the figure. Note that full profiles are shown in panels a–c and outliers have not been removed; this provides a sense of the typical variation that is observed within the Martian ionosphere and LPW data set. Variations are comparable between all line colors; however, overall profile shapes of the red and green lines are significantly different to the gray ones.

From the statistical study presented in Figure 8 one can see that orbit segments during which larger amplitude magnetosonic wave-like features were observed (indicated by the red and green profiles) show large differences in ionospheric electron density above altitudes of about 250 km, compared to orbits where no wave-like activity was observed. The green and red lines in panel a (which had the largest accompanying wave amplitudes) show that ionospheric densities are reduced by almost 2 orders of magnitude above 350-km altitude, compared to gray orbits. Blue lines (which showed smaller-amplitude magnetosonic wave-like behavior) show similar behavior, albeit usually not as extreme as the green and red orbits. Panel a clearly shows that the upper ionosphere has been severely eroded when magnetosonic-like waves are observed, suggesting that the ion heating and energization discussed in section 4.4 can lead to substantial ion outflow in the upper ionosphere. Electron temperatures for the red and green profiles appear elevated above about 300 km (panel b), and the fact that these temperatures become so hot above this altitude that they cannot be derived from LPW measurements supports the idea that significant ionospheric heating and/or erosion is occurring during these orbits.

Because the underlying neutral density is the primary source of the ionosphere it is also important to compare neutral density profiles between orbits. Panel c shows that the total neutral density is slightly lower for the green profile, compared to the gray ones, above about 250-km altitude. It is unlikely that this difference could produce the extreme erosion observed in ionospheric density. This is supported by the fact that several red profiles demonstrate enhanced neutral densities above 250 km. Subsequently, we leave an in-depth investigation of the effects of the neutral atmosphere on atmospheric erosion to a later study.

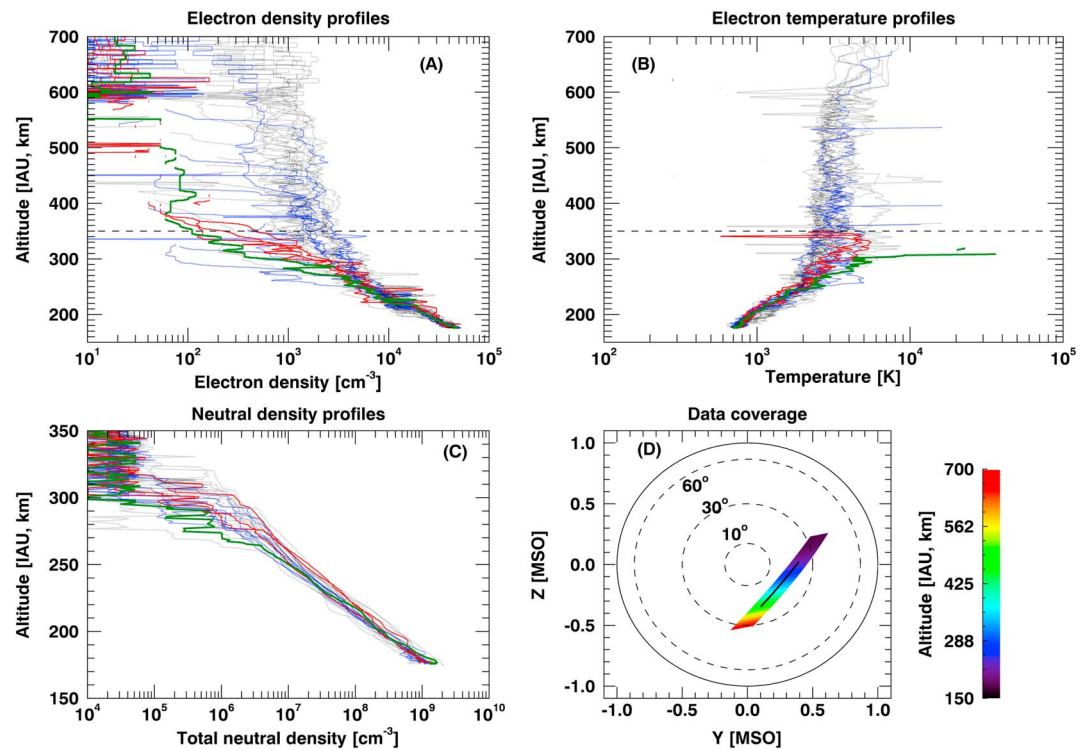


**Figure 8.** Various profiles for 29 orbits neighboring the pass shown in Figure 1, equivalent to roughly 3 days before and after that pass. Panel a shows Langmuir Probe and Wave  $N_e$  profiles as a function of altitude. The colored lines show various levels of magnetosonic wave behavior that were present: gray: no waves; blue: small-amplitude waves ( $<10$  nT); red: large-amplitude waves (10–20 nT); green: the event in Figure 1 (25 nT). Panels b and c show the corresponding Langmuir Probe and Wave  $T_e$  and Neutral Gas and Ion Mass Spectrometer total neutral density profiles for these orbits, to the same color code. Panel d shows the coverage of these orbits projected on the Y-Z Mars Solar Orbital (MSO) plane. The pass shown in Figure 1 is marked by the solid black line. IAU = International Astronomical Union.

## 6. General Discussion

The magnetosonic waves investigated in this study are thought to be driven by the planet-solar wind interaction, and demonstrate that similar magnetosonic waves can propagate planetward through the Martian foreshock and magnetosheath regions. Severe ionospheric erosion occurs for the event studied here demonstrating that such waves can be a significant driver of ionospheric structure, energy, and outflow at Mars. Future work will attempt to estimate the ion outflow rates driven by these waves, although complexities exist in achieving this. The ion outflow rate will be limited by how quickly the eroded ionosphere can refill, for example. Figure 8 demonstrates that the ionosphere is severely eroded just above the Martian exobase, and the ion outflow rate will become limited because ionospheric plasma must pass through the exobase region to replenish that lost above.

The magnetosonic wave event investigated here demonstrates that compressional wave modes can be produced by the unmagnetized planet-solar wind interaction and that these wave modes can significantly heat the dayside ionosphere, directly leading to ion outflow. In comparison, at Earth (a magnetized planet), ion outflow is typically driven by a multistep process and occurs primarily in the polar cusp regions (e.g., André & Yau, 1997). Ions must first gain enough thermal energy to upwell such that they may encounter waves or potential drops at higher altitudes. Such ions may be accelerated upward along the terrestrial dipole magnetic field by potential drops or may experience wave heating perpendicular to the local magnetic field. The converging nature of the magnetic field in the polar cusp regions means that perpendicularly heated ions can experience an upward directed ponderomotive force. Both mechanisms drive substantial ion outflow at Earth. In contrast, at smaller-unmagnetized bodies such as Mars and likely Venus, it appears that waves created by the planet-solar wind interaction can propagate into the ionosphere and deposit substantial amounts of energy there, leading to direct ion outflow.

Compressional wave modes similar to those studied here have also been observed at Comet P/Halley (e.g., Glassmeier et al., 1993; Mazelle et al., 1989, 1991; Mazelle & Neubauer, 1993), suggesting that such waves may represent a fundamental element of the solar wind interaction with unmagnetized bodies. Transverse wave mode heating is also known to occur within the dayside Venusian ionosphere (Scarf et al., 1980; Taylor et al., 1979) and has been suggested as a source for ionospheric heating at Mars (e.g., Ergun et al., 2006; Fowler, Andersson, Peterson, et al., 2017; Fowler, Ergun, et al., 2017). Thus, the solar wind interaction with unmagnetized bodies in general appears to produce a variety of wave modes that can propagate into the ionospheres of these bodies and deposit significant amounts of energy there.

The observed large-amplitude magnetosonic waves have been shown to drive significant erosion of the Martian ionosphere (Figure 8). Key limitations on how much of the ionosphere can be eroded include the time scale for replenishment of the ionosphere and how frequently these large-amplitude magnetosonic wave events occur. If such events were to occur frequently in the past then this ionospheric heating mechanism may have significant implications for the long-term atmospheric and climatic evolution of Mars and at other unmagnetized bodies in the solar system.

## 7. Conclusions

Large-amplitude magnetosonic waves at a frequency of about 0.035 Hz are observed to propagate from the magnetosheath into the deep dayside ionosphere at Mars. These waves reach magnitudes of  $\sim 25$  nT, which is about 40% of the background magnetic field strength. In the upper ionosphere, the amplitudes of these waves increase as they propagate downward, matching the quantitative predictions that are expected for such a magnetosonic wave propagating into an increasingly dense, charged medium. When the waves encounter the dense,  $O_2^+$  dominated ionosphere, they are efficiently damped. The estimated wavelengths of these waves are significantly larger than typical gradient length scales in the Martian ionosphere, and we envision these waves as individual fronts “crashing” through the ionosphere, much like waves breaking on a beach, as opposed to wave trains propagating through the ionosphere.

The compressional wave fronts drive large variations in the suprathermal electron density and temperature, and lighter ion species ( $H^+$ ) densities. Variations in the ionospheric electron density, and heavy ion densities ( $O^+$  and  $O_2^+$ ), also occur but are not in phase with the compressional wave fronts. These density and temperature variations range in amplitude from  $\sim 20\%$  to 100%.

Whistler waves are observed during times of enhanced magnetic field strength (i.e., compressional wave fronts), and these Whistler waves are likely produced by unstable, anisotropic suprathermal electron populations. The suprathermal electrons are driven anisotropic by the propagation of magnetosonic wave fronts through the ionosphere.

When damping of the magnetosonic waves occurs in the dense,  $O_2^+$  dominated ionosphere, significant ion heating is correspondingly observed. Ion temperatures derived from ion velocity distributions show that  $O^+$  and  $O_2^+$  temperatures of  $\sim 5$ –10 eV are observed just above the Martian exobase. The most intense wave damping occurs when the ionospheric composition transitions to a predominantly  $O_2^+$  one and a quantitative analysis based on the MAVEN observations leads to estimates of ion heating rates between 0.03 and 0.2 eV/s<sup>-1</sup> per ion here. The  $O_2^+$  gyroperiod is slightly lower than the magnetosonic wave frequency, suggesting that the background magnetic field strength and ionospheric composition are important for determining the damping rate of the magnetosonic wave. Ions exposed to these heating rates can subsequently gain escape energy in  $\sim 10$ –70 s, and such heating may lead to substantial ion outflow to space.

## Appendix A: Deriving Ion Temperature From Ion Velocity Distributions

By assuming that the ion populations observed within Figure 6 are Maxwellian, ion temperatures can be derived for each species by fitting a straight line to the natural logarithm of the ion distribution function, as a function of ion energy, along the “ridge” of the distribution. The inverse of the gradient of this straight line represents the ion temperature,  $T_i$ . The straight black lines in panels a–c show the ridges of each distribution, determined by eye. The blue crosses mark data points in the interpolated grid that lie closest to this line, and which were used to derive  $T_i$  for each distribution. Many of the populations observed in this study appear to have hot tail populations which are not included in the derivation of  $T_i$ .

The vertical error bars for distribution function shown in Figures 6d–6f are estimated by plotting the maximum and minimum distribution function values found an interpolated grid point either side of the primary measurement point in the corresponding contour plots in panels a–c. The lower and upper best fit estimates for the derived  $T_i$  are based upon a 30% increase in the fit residual value, when  $T_i$  is increased and decreased from its best fit value. These limits are shown in panels d–f as the blue and red lines, respectively.

Due to ongoing STATIC instrument calibration, ions with energies less than 5 eV were not included in the fitting, and this limit was sometimes raised such that only the linear portion of the distribution function in this plotting format was fitted to. A similar method is described in more detail in Sharp et al. (1983) and has recently been used to estimate  $T_i$  in other studies of MAVEN STATIC data (Fowler, Ergun, et al., 2017).

Estimated  $T_i$  is not available at all time steps for all ion species because the fitting method requires a significant number of ions be present whose temperatures are warmer than a few electron volts. Protons do not represent a significant fraction of the ion population past about 05:55:30, and proton temperatures cannot be derived after this time.  $O^+$  and  $O_2^+$  temperatures become too cold to be derived using this method past about 05:57.

### Acknowledgments

Work at LASP and SSL was supported by NASA funding for the MAVEN project through the Mars Exploration Program under grant NNH10CC04C. Data used in this study are available on the NASA Planetary Data System via <https://pds.nasa.gov/>. We thank Tristan Weber for useful discussions interpreting SWEA data. Wavelet software was provided by C. Torrence and G. Compo and is available at URL: <http://paos.colorado.edu/research/wavelets/>.

### References

- Andersson, L., Ergun, R., Delory, G., Eriksson, A., Westfall, J., Reed, H., et al. (2015). The Langmuir probe and waves (LPW) instrument for MAVEN. *Space Science Reviews*, 195(1–4), 173–198. <https://doi.org/10.1007/s11214-015-0194-3>
- André, M., & Yau, A. (1997). Theories and observations of ion energization and outflow in the high latitude magnetosphere. In B., Hultqvist, & M., Øieroset (Eds.), *Transport Across the Boundaries of the Magnetosphere* (pp. 27–48). Bern, Switzerland: Springer.
- Bertucci, C., Duru, F., Edberg, N., Fraenz, M., Martinecz, C., Szego, K., & Vaisberg, O. (2011). The induced magnetospheres of Mars, Venus, and Titan. *Space Science Reviews*, 162(1–4), 113–171. <https://doi.org/10.1007/s11214-011-9845-1>
- Bertucci, C., Mazelle, C., & Acuña, M. H. (2005). Interaction of the solar wind with Mars from Mars Global Surveyor MAG/ER observations. *Journal of Atmospheric and Solar-Terrestrial Physics*, 67(17–18), 1797–1808. <https://doi.org/10.1016/j.jastp.2005.04.007>
- Bertucci, C., Mazelle, C., Crider, D., Mitchell, D., Sauer, K., Acuña, M., et al. (2004). MGS MAG/ER observations at the magnetic pileup boundary of Mars: Draping enhancement and low frequency waves. *Advances in Space Research*, 33(11), 1938–1944. <https://doi.org/10.1016/j.asr.2003.04.054>
- Bertucci, C., Mazelle, C., Crider, D. H., Vignes, D., Acuña, M. H., Mitchell, D. L., et al. (2003). Magnetic field draping enhancement at the Martian magnetic pileup boundary from Mars global surveyor observations. *Geophysical Research Letters*, 30(2), 1099. <https://doi.org/10.1029/2002GL015713>
- Brain, D. A., Bagenal, F., Acuña, M. H., Connerney, J. E. P., Crider, D. H., Mazelle, C., et al. (2002). Observations of low-frequency electromagnetic plasma waves upstream from the Martian shock. *Journal of Geophysical Research*, 107(A6), SMP 9-1–SMP 9-1. <https://doi.org/10.1029/2000JA000416>
- Brain, D. A., Mitchell, D. L., & Halekas, J. S. (2006). The magnetic field draping direction at Mars from April 1999 through August 2004. *Icarus*, 182(2), 464–473. <https://doi.org/10.1016/j.icarus.2005.09.023>
- Cloutier, P., & Daniell, Jr. R. E. (1979). An electrodynamic model of the solar wind interaction with the ionospheres of Mars and Venus. *Planetary and Space Science*, 27(8), 1111–1121. [https://doi.org/10.1016/0032-0633\(79\)90082-5](https://doi.org/10.1016/0032-0633(79)90082-5)
- Cloutier, P., Law, C., Crider, D., Walker, P., Chen, Y., Acuña, M., et al. (1999). Venus-like interaction of the solar wind with Mars. *Geophysical Research Letters*, 26(17), 2685–2688. <https://doi.org/10.1029/1999GL005051>
- Cloutier, P., McElroy, M., & Michel, F. (1969). Modification of the Martian ionosphere by the solar wind. *Journal of Geophysical Research*, 74(26), 6215–6228. <https://doi.org/10.1029/JA074i026p06215>
- Connerney, J., Espley, J., DiBraccio, G., Gruesbeck, J., Oliverson, R., Mitchell, D., et al. (2015). First results of the MAVEN magnetic field investigation. *Geophysical Research Letters*, 42, 8819–8827. <https://doi.org/10.1002/2015GL065366>
- Connerney, J. E. P., Espley, J., Lawton, P., Murphy, S., Odom, J., Oliverson, R., & Sheppard, D. (2015). The MAVEN Magnetic Field Investigation. *Space Science Reviews*, 195(1–4), 257–291. <https://doi.org/10.1007/s11214-015-0169-4>
- Dubinin, E., & Fraenz, M. (2016). Ultra-low-frequency waves at Venus and Mars. *Low-Frequency Waves in Space Plasmas*, 216, 343–364. <https://doi.org/10.1002/9781119055006.ch20>
- Dubinin, E., Modolo, R., Fraenz, M., Woch, J., Duru, F., Akalin, F., et al. (2008). Structure and dynamics of the solar wind/ionosphere interface on Mars: MEX-ASPERA-3 and MEX-MARSIS observations. *Geophysical Research Letters*, 35, L11103. <https://doi.org/10.1029/2008GL033730>
- Edberg, N. J. T., Lester, M., Cowley, S. W. H., & Eriksson, A. I. (2008). Statistical analysis of the location of the Martian magnetic pileup boundary and bow shock and the influence of crustal magnetic fields. *Journal of Geophysical Research*, 113, a08206. <https://doi.org/10.1029/2008JA013096>
- Edberg, N., Nilsson, H., Williams, A., Lester, M., Milan, S., Cowley, S., et al. (2010). Pumping out the atmosphere of Mars through solar wind pressure pulses. *Geophysical Research Letters*, 37, L03107. <https://doi.org/10.1029/2009GL041814>
- Ergun, R., Andersson, L., Peterson, W., Brain, D., Delory, G., Mitchell, D., et al. (2006). Role of plasma waves in Mars' atmospheric loss. *Geophysical Research Letters*, 33, L14103. <https://doi.org/10.1029/2006GL025785>
- Ergun, R., Morooka, M., Andersson, L., Fowler, C., Delory, G., Andrews, D. J., et al. (2015). Dayside electron temperature and density profiles at Mars: First results from the MAVEN Langmuir probe and waves instrument. *Geophysical Research Letters*, 42, 8846–8853. <https://doi.org/10.1002/2015GL065280>
- Espley, J. R., Delory, G. T., & Cloutier, P. A. (2006). Initial observations of low-frequency magnetic fluctuations in the Martian ionosphere. *Journal of Geophysical Research*, 111, e06522. <https://doi.org/10.1029/2005JE002587>
- Fowler, C. M., Andersson, L., Halekas, J., Espley, J. R., Mazelle, C., Coughlin, E. R., et al. (2017). Electric and magnetic variations in the near-Mars environment. *Journal of Geophysical Research: Space Physics*, 122, 8536–8559. <https://doi.org/10.1002/2016JA023411>
- Fowler, C., Andersson, L., Peterson, W., Halekas, J., Nagy, A., Ergun, R., et al. (2017). Correlations between enhanced electron temperatures and electric field wave power in the Martian ionosphere. *Geophysical Research Letters*, 45, 493–501. <https://doi.org/10.1002/2017GL073387>
- Fowler, C. M., Ergun, R. E., Andersson, L., Peterson, W. K., Hara, T., McFadden, J., et al. (2017). Ion heating in the Martian ionosphere. *Journal of Geophysical Research: Space Physics*, 122, 10,612–10,625. <https://doi.org/10.1002/2017JA024578>

- Futaana, Y., Barabash, S., Yamauchi, M., McKenna-Lawlor, S., Lundin, R., Luhmann, J., et al. (2008). Mars Express and Venus Express multi-point observations of geoeffective solar flare events in December 2006. *Planetary and space science*, *56*(6), 873–880. <https://doi.org/10.1016/j.pss.2007.10.014>
- Glassmeier, K.-H., Motschmann, U., Mazelle, C., Neubauer, F. M., Sauer, K., Fuselier, S., & Acuna, M. (1993). Mirror modes and fast magnetoacoustic waves near the magnetic pileup boundary of comet P/Halley. *Journal of Geophysical Research*, *98*(A12), 20,955–20,964. <https://doi.org/10.1029/93JA02582>
- Halekas, J., Brain, D., & Eastwood, J. (2011). Large-amplitude compressive “sawtooth” magnetic field oscillations in the Martian magnetosphere. *Journal of Geophysical Research*, *116*, A07222. <https://doi.org/10.1029/2011JA016590>
- Halekas, J., Taylor, E., Dalton, G., Johnson, G., Curtis, D., McFadden, J., et al. (2015). The solar wind ion analyzer for MAVEN. *Space Science Reviews*, *195*(1–4), 125–151. <https://doi.org/10.1007/s11214-013-0029-z>
- Harada, Y., Andersson, L., Fowler, C., Mitchell, D., Halekas, J., Mazelle, C., et al. (2016). MAVEN observations of electron-induced whistler mode waves in the Martian magnetosphere. *Journal of Geophysical Research: Space Physics*, *121*, 9717–9731. <https://doi.org/10.1002/2016JA023194>
- Jakosky, B. M., Lin, R., Grebowsky, J., Luhmann, J., Mitchell, D., Beutelschies, G., et al. (2015). The Mars Atmosphere and Volatile Evolution (MAVEN) mission. *Space Science Reviews*, *195*(1–4), 3–48. <https://doi.org/10.1007/s11214-015-0139-x>
- Kennel, C. F., & Petschek, H. (1966). Limit on stably trapped particle fluxes. *Journal of Geophysical Research*, *71*(1), 1–28. <https://doi.org/10.1029/JZ071i001p00001>
- Lundin, R., Barabash, S., Andersson, H., Holmström, M., Grigoriev, A., Yamauchi, M., et al. (2004). Solar wind-induced atmospheric erosion at Mars: First results from ASPERA-3 on Mars Express. *science*, *305*(5692), 1933–1936. <https://doi.org/10.1126/science.1101860>
- Lundin, R., Barabash, S., Dubinin, E., Winningham, D., & Yamauchi, M. (2011). Low-altitude acceleration of ionospheric ions at Mars. *Geophysical Research Letters*, *38*, L08108. <https://doi.org/10.1029/2011GL047064>
- Lundin, R., Barabash, S., Holmström, M., Nilsson, H., Yamauchi, M., Fraenz, M., & Dubinin, E. (2008). A comet-like escape of ionospheric plasma from Mars. *Geophysical Research Letters*, *35*, L18203. <https://doi.org/10.1029/2008GL034811>
- Mahaffy, P. R., Benna, M., King, T., Harpold, D. N., Arvey, R., Barciniak, M., et al. (2015). The neutral gas and ion mass spectrometer on the Mars atmosphere and volatile evolution mission. *Space Science Reviews*, *195*(1–4), 49–73. <https://doi.org/10.1007/s11214-014-0091-1>
- Mazelle, C., Belmont, G., Glassmeier, K.-H., Le Queau, D., & Reme, H. (1991). Ultra low frequency waves at the magnetic pile-up boundary of comet P/Halley. *Advances in Space Research*, *11*(9), 73–77. [https://doi.org/10.1016/0273-1177\(91\)90014-B](https://doi.org/10.1016/0273-1177(91)90014-B)
- Mazelle, C., & Neubauer, F. M. (1993). Discrete wave packets at the proton cyclotron frequency at comet P/Halley. *Geophysical Research Letters*, *20*(2), 153–156. <https://doi.org/10.1029/92GL02613>
- Mazelle, C., Reme, H., Sauvaud, J., d’Uston, C., Carlson, C., Anderson, K., et al. (1989). Analysis of suprathermal electron properties at the magnetic pile-up boundary of comet P/Halley. *Geophysical Research Letters*, *16*(9), 1035–1038. <https://doi.org/10.1029/GL016i009p01035>
- McFadden, J., Kortmann, O., Curtis, D., Dalton, G., Johnson, G., Abiad, R., et al. (2015). MAVEN suprathermal and thermal ion composition (STATIC) instrument. *Space Science Reviews*, *195*(1–4), 199–256. <https://doi.org/10.1007/s11214-015-0175-6>
- Mitchell, D., Mazelle, C., Sauvaud, J.-A., Thocaven, J.-J., Rouzaud, J., Fedorov, A., et al. (2016). The MAVEN solar wind electron analyzer. *Space Science Reviews*, *200*(1–4), 495–528. <https://doi.org/10.1007/s11214-015-0232-1>
- Mittelholz, A., Johnson, C. L., & Lillis, R. J. (2017). Global-scale external magnetic fields at Mars measured at satellite altitude. *Journal of Geophysical Research: Planets*, *122*, 1243–1257. <https://doi.org/10.1002/2017JE005308>
- Morschhauser, A., Lesur, V., & Grott, M. (2014). A spherical harmonic model of the lithospheric magnetic field of Mars. *Journal of Geophysical Research: Planets*, *119*, 1162–1188. <https://doi.org/10.1002/2013JE004555>
- Moses, S., Coroniti, F., & Scarf, F. (1988). Expectations for the microphysics of the Mars-solar wind interaction. *Geophysical Research Letters*, *15*(5), 429–432. <https://doi.org/10.1029/GL015i005p00429>
- Papadopoulos, K. (1971). Ion thermalization in the Earth’s bow shock. *Journal of Geophysical Research*, *76*(16), 3806–3810. <https://doi.org/10.1029/JA076i016p03806>
- RiOUSset, J. A., Paty, C. S., Lillis, R. J., Fillingim, M. O., England, S. L., Withers, P. G., & Hale, J. P. (2014). Electrodynamics of the Martian dynamo region near magnetic cusps and loops. *Geophysical Research Letters*, *41*, 1119–1125. <https://doi.org/10.1002/2013GL059130>
- Scarf, F., Taylor, W., Russell, C., & Elphic, R. (1980). Pioneer Venus plasma wave observations: The solar wind-Venus interaction. *Journal of Geophysical Research*, *85*(A13), 7599–7612. <https://doi.org/10.1029/JA085iA13p07599>
- Schunk, R., & Nagy, A. (2009). *Ionospheres: Physics, plasma physics, and chemistry*. UK: Cambridge University Press.
- Sharp, R., Lennartsson, W., Peterson, W., & Ungstrup, E. (1983). The mass dependence of wave particle interactions as observed with the ISEE-1 energetic ion mass spectrometer. *Geophysical Research Letters*, *10*(8), 651–654. <https://doi.org/10.1029/GL010i008p00651>
- Slavin, J., Schwingschuh, K., Riedler, W., & Yeroshenko, Y. (1991). The solar wind interaction with Mars: Mariner 4, Mars 2, Mars 3, Mars 5, and Phobos 2 observations of bow shock position and shape. *Journal of Geophysical Research*, *96*(A7), 11,235–11,241. <https://doi.org/10.1029/91JA00439>
- Taylor, W., Scarf, F., Russell, C., & Brace, L. (1979). Absorption of whistler mode waves in the ionosphere of Venus. *Science*, *205*(4401), 112–114. <https://doi.org/10.1126/science.205.4401.112>
- Torrence, C., & Compo, G. P. (1998). A practical guide to wavelet analysis. *Bulletin of the American Meteorological society*, *79*(1), 61–78. [https://doi.org/10.1175/1520-0477\(1998\)079<0061:APGTWA>2.0.CO;2](https://doi.org/10.1175/1520-0477(1998)079<0061:APGTWA>2.0.CO;2)
- Vignes, D., Mazelle, C., Rme, H., Acu-a, M. H., Connerney, J. E. P., Lin, R. P., et al. (2000). The solar wind interaction with Mars: Locations and shapes of the bow shock and the magnetic pile-up boundary from the observations of the MAG/ER Experiment onboard Mars Global Surveyor. *Geophysical Research Letters*, *27*(1), 49–52. <https://doi.org/10.1029/1999GL010703>
- Winningham, J., Frahm, R., Sharber, J., Coates, A., Linder, D., Soobiah, Y., et al. (2006). Electron oscillations in the induced Martian magnetosphere. *Icarus*, *182*(2), 360–370. <https://doi.org/10.1016/j.icarus.2005.10.033>